OXFORD

Single voxel autocorrelation uncovers gradients of temporal dynamics in the hippocampus and entorhinal cortex during rest and navigation

Nichole R. Bouffard [1,2,*,†], Ali Golestani[1,†], Iva K. Brunec[3,4], Buddhika Bellana[5], Jun Young Park[1,6], Morgan D. Barense[1,2,‡],

Morris Moscovitch[1,2,‡]

[1]Department of Psychology, University of Toronto, Sidney Smith Hall, 100 St. George Street, Toronto, ON M5S 3G3, Canada,
[2]Rotman Research Institute, Baycrest Health Sciences, 3650 Baycrest Street, Toronto, ON M6A 2E1, Canada,
[3]Department of Psychology, Temple University, 1701 North 13th Street, Philadelphia, PA 19122, USA,
[4]Department of Psychology, University of Pennsylvania, 3720 Walnut Street, Philadelphia, PA 19104, USA,
[5]Department of Psychology, Glendon College—York University, 2275 Bayview Ave, North York, ON M4N 3M6, Canada,
[6]Department of Statistical Sciences, University of Toronto, Sidney Smith Hall, 100 St. George Street, Toronto, ON M5S 3G3, Canada

*Corresponding author: Department of Psychology, University of Toronto, Sidney Smith Hall, 100 St. George Street, Toronto, ON M5S 3G3, Canada.
Email: nichole.bouffard@mail.utoronto.ca

[†]Nichole R. Bouffard and Ali Golestani contributed equally.
[‡]Morgan D. Barense and Morris Moscovitch are shared senior authorship.

During navigation, information at multiple scales needs to be integrated. Single-unit recordings in rodents suggest that gradients of temporal dynamics in the hippocampus and entorhinal cortex support this integration. In humans, gradients of representation are observed, such that granularity of information represented increases along the long axis of the hippocampus. The neural underpinnings of this gradient in humans, however, are still unknown. Current research is limited by coarse fMRI analysis techniques that obscure the activity of individual voxels, preventing investigation of how moment-to-moment changes in brain signal are organized and how they are related to behavior. Here, we measured the signal stability of single voxels over time to uncover previously unappreciated gradients of temporal dynamics in the hippocampus and entorhinal cortex. Using our novel, single voxel autocorrelation technique, we show a medial-lateral hippocampal gradient, as well as a continuous autocorrelation gradient along the anterolateral-posteromedial entorhinal extent. Importantly, we show that autocorrelation in the anterior-medial hippocampus was modulated by navigational difficulty, providing the first evidence that changes in signal stability in single voxels are relevant for behavior. This work opens the door for future research on how temporal gradients within these structures support the integration of information for goal-directed behavior.

Key words: hippocampus; entorhinal cortex; autocorrelation; gradients; navigation.

Introduction

To enable efficient goal-directed behavior, information must be represented and integrated across multiple temporal and spatial scales. It has been proposed that neural signal gradients in the hippocampus and entorhinal cortex support such multiscale representations in rodents, but evidence in humans is sparse and has methodological limitations. Previously, fMRI analysis techniques have uncovered local signal gradients in the human hippocampus (Brunec, Bellana, et al. 2018). These investigations, however, have been limited by analyzing patterns of activity across relatively coarse regions of interest (ROIs), making it unclear how sustained versus rapidly changing signals are distributed throughout the hippocampus. Many of these analyses use predetermined anterior and posterior anatomical masks, which limit our ability to detect neural signal gradients in an unsupervised way, therefore preventing us from investigating gradients that exist along both anterior–posterior and medial-lateral axes of the hippocampus. Moreover, there have been no prior investigations of autocorrelation gradients in the entorhinal cortex, despite its key role in spatial and temporal representations during navigation. To address these limitations, we have developed a novel, data-driven analysis

based on autocorrelation of single voxels in fMRI during rest and navigation. This technique allows us, for the first time, to track the signal stability of individual voxels and their spatial distribution in an unconstrained way along both the anterior–posterior and medial-lateral axes of the hippocampus and entorhinal cortex. Based on this single voxel analysis, we uncover gradients of neural signal dynamics along these axes in both structures and relate them to behavior.

In rodents, place fields in the ventral hippocampus (homologous to the anterior hippocampus in humans) span larger areas, show a higher degree of overlap, and higher correlation in their firing across time, compared with the dorsal hippocampus (homologous to the posterior hippocampus in humans) (Jung et al. 1994; Hasselmo 2008; Kjelstrup et al. 2008; Komorowski et al. 2013). A similar gradient of hippocampal organization is also observed in the human hippocampus. Tracking moment-to-moment similarity across patterns of voxels during virtual navigation, Brunec, Bellana, et al. (2018) found that signal similarity was significantly greater within the anterior hippocampus relative to the posterior hippocampus, indicating that, as in the rodent ventral hippocampus, the human anterior hippocampus demonstrates

slower changing signals that are sustained across time and space. These results suggest that a relatively stable pattern of activity in the rodent and human hippocampus follows a scaled gradient, from faster changing signal in the posterior (dorsal) hippocampus to slower changing signal in the anterior (ventral) hippocampus. This gradient organization might underlie fine-to-coarse mnemonic representation, particularly when a different granularity of information needs to be maintained across time (Robin and Moscovitch 2017; Brunec and Momennejad 2022). In addition to the dorsal-ventral gradient of spatial representation observed in rodents, research suggests a difference in spatial selectivity along the proximodistal axis (homologous to medial-lateral in humans), specifically in CA1 (Igarashi et al. 2014), yet whether a similar medial-lateral distinction exists in the human hippocampus is still unclear (Hrybouski et al. 2019).

A key input structure to the hippocampus that has been implicated in integrating information over time during navigation is the entorhinal cortex. Prior research has found distinct functional differentiation between the anterolateral and posteromedial aspects of the human entorhinal cortex (ERC), including a few prior investigations of neural signal gradients in the ERC (Evensmoen et al. 2015; Maass et al. 2015; Navarro Schröder et al. 2015; Syversen et al. 2021). The lateral ERC in rodents, and the homologous anterolateral ERC in humans, supports within-object and object-location coding, as well as temporal information processing (Olsen et al. 2017; Yeung et al. 2017, 2019; Tsao et al. 2018; Bellmund et al. 2019; Montchal et al. 2019). In contrast, the posteromedial ERC in humans has been primarily linked to scene processing (Maass et al. 2015; Navarro Schröder et al. 2015; Berron et al. 2018) and related to grid cell organization (Bellmund et al. 2016), consistent with evidence of grid cells in the medial ERC in rodents (Hafting et al. 2005). Given prior evidence of functional distinctions of the ERC into anterolateral and posteromedial regions, we developed a data-driven method to directly probe whether there exists a continuous neural signal gradient in both the anterior–posterior and medial-lateral axes of this structure. Investigating these regions in tandem within the same analytic framework is also motivated by evidence of strong reciprocal connectivity between the hippocampus and ERC (Small et al. 2011; Maass et al. 2015; Dalton et al. 2019, 2021).

To understand how a graded organization of signal dynamics in the hippocampus and ERC supports goal-directed behavior, we developed an analytic approach of temporal autocorrelation at the single voxel level, which we implemented during both rest and navigation. Electrophysiology studies in rodents find that neurons within the hippocampus demonstrate firing patterns that are maintained across time (i.e. temporal autocorrelation) and space (i.e. spatial autocorrelation) as the rodent traverses a track (Jung et al. 1994; Hasselmo 2008; Kjelstrup et al. 2008; Komorowski et al. 2013). Because recording from single units or populations of neurons in vivo in humans is challenging and not always feasible, we developed an analytic approach in which we can measure neural signal similarity over time, or autocorrelation, in single voxels and relate it to behavior. Temporal autocorrelation in fMRI represents the degree of similarity between the BOLD signal and the temporally shifted, or lagged, version of the signal over successive time intervals (Fig. 1A). Conventionally, it is assumed that this autocorrelation in fMRI data originates from physical and physiological noise (Purdon and Weisskoff 1998; Bullmore et al. 2001; Lund et al. 2006; Lenoski et al. 2008; Arbabshirani et al. 2014; Bollmann et al. 2018; James et al. 2019) or the hemodynamic response function (HRF; Rajapakse et al. 1998; Arbabshirani et al. 2014; James et al. 2019) and, therefore, has been considered

irrelevant to brain function. Recently, however, Arbabshirani et al. (2019) found that autocorrelation reflects changes in cognitive state (task vs. rest) as well as changes in mental state (healthy control vs. schizophrenia), suggesting that the observed changes in the autocorrelation are also modulated by cognitive processes. Prior studies, however, have been limited and are unable to answer the question of how temporal autocorrelation is directly related to behavior. Examining the temporal autocorrelation[1] of single voxels during an active navigation task, therefore, is important for understanding how a stable, highly correlated signal is relevant for behavior.

Investigating the fMRI signal at the single voxel level allows us to measure neural gradients with more precision than previous methods. While studies with fMRI in humans suggest that functional heterogeneity exists along the long axis of the hippocampus (Nadel et al. 2013; Poppenk et al. 2013; see Grady 2020 for a review) and the anterior–posterior and medial-lateral extents of the ERC (e.g. Hafting et al. 2005; Maass et al. 2015; Navarro Schröder et al. 2015), many of the previous analysis techniques have been limited to investigations using predetermined anatomical masks, which obscures the contribution of individual voxels, making it unclear whether graded signals extend along multiple axes in these regions. There have been a few studies that have employed more precise techniques, such as investigating hippocampal and entorhinal gradients slice-by-slice (Evensmoen et al. 2015) or using voxelwise connectivity approaches (Navarro Schröder et al. 2015; Syversen et al. 2021). These studies converge on the idea that there are continuous functional connectivity gradients along the hippocampal long axis and the anterolateral to posteromedial entorhinal extent defined by connectivity to other regions in the brain, but it is still unknown how the internal dynamics within these regions are distributed and how the signal profiles of individual voxels are organized throughout the hippocampus and entorhinal cortex. Examining the autocorrelation at the single voxel level, therefore, allows for a finer grained analysis that may be more sensitive to differences in navigational performance and can help us to determine how a scaled gradient of signal similarity might be employed to integrate representations across spatial scales during navigation. We, therefore, combine our single voxel autocorrelation approach with an unconstrained clustering method to determine how temporal autocorrelation is distributed in multiple dimensions throughout the hippocampus and ERC.

Here, we present evidence of a functional medial-lateral neural signal gradient in the hippocampus as well as a novel continuous gradient in the ERC. Using resting state fMRI data with high spatial and temporal resolution from the Human Connectome Project (HCP) (Dataset 1), we measured single voxel autocorrelation in the hippocampus and ERC. Using task-based fMRI (with lower spatial resolution), we measured the single voxel autocorrelation in the hippocampus, while participants completed a real-world navigation task (Dataset 2). We measured the similarity of single voxels over time by correlating the timecourse of each voxel with temporally shifted versions of itself (Fig. 1A). We applied data-driven clustering to determine how temporal autocorrelation was spatially distributed throughout the hippocampus and ERC (Fig. 1B and C). We reasoned that there were three plausible mechanisms that might drive distinct autocorrelation

---

[1] We chose temporal autocorrelation to calculate the similarity of a signal to a lagged version of itself. Other signal "self-similarity" metrics in the time domain (e.g. autoregressive model (López-Madrona et al. 2019) or frequency domain (e.g. power-law exponent (He 2014) can alternatively be used. Nevertheless, we expect to observe the same findings, as these "self-similarity" measures are highly correlated.
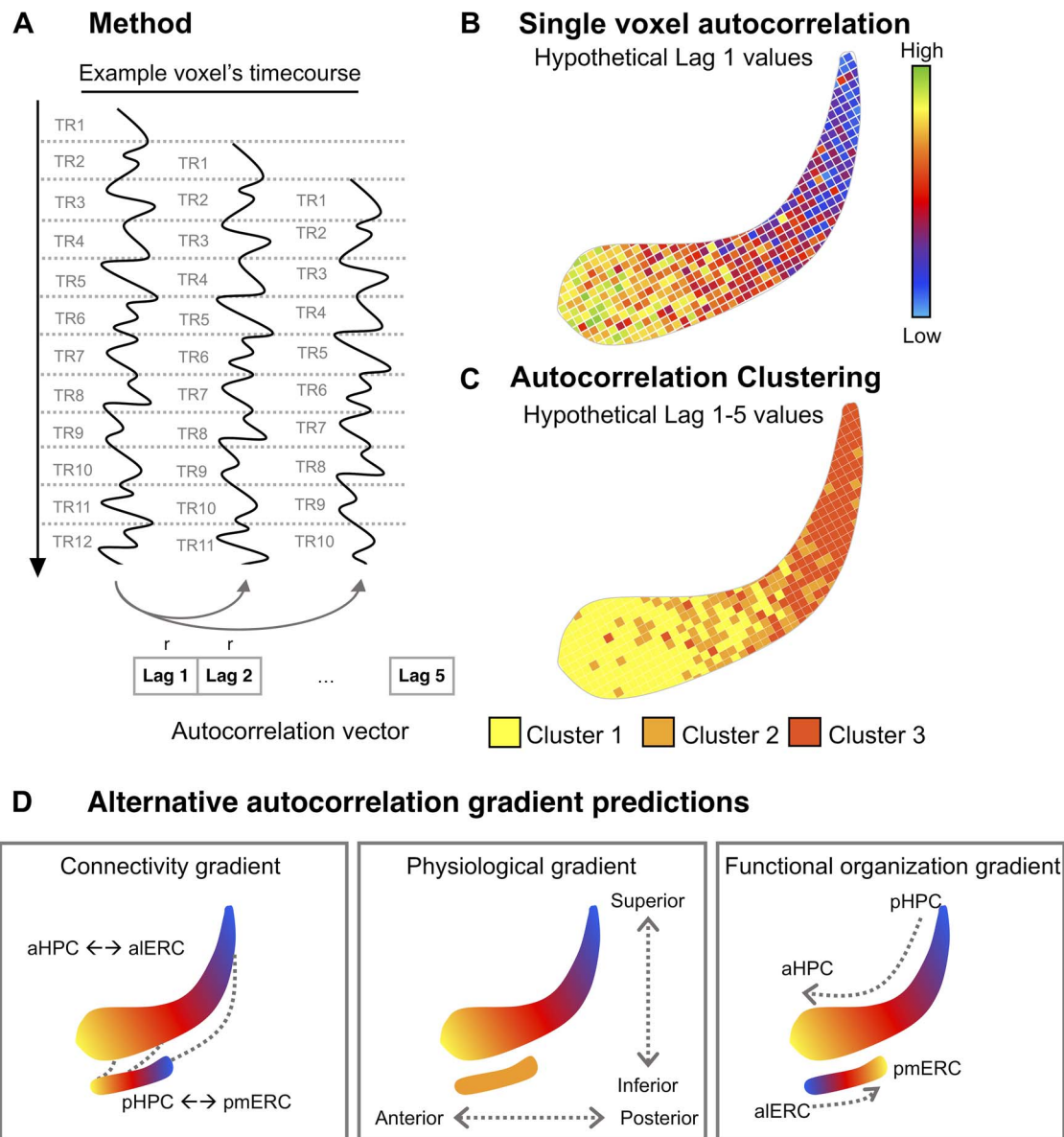
Fig. 1. A) Method. For each voxel, the timecourse of activity was successively temporally shifted by 1 TR and correlated with itself. This was repeated for a total shift of 4 s (i.e. 5 lags for resting state data [Dataset 1] and 2 lags for navigation data [Dataset 2]). This resulted in a vector of single voxel autocorrelation values, with each value corresponding to a different lagged correlation. **B) Single voxel autocorrelation (hypothetical values).** The procedure was repeated for all voxels in an ROI. To examine the spatial distribution of the single voxel autocorrelation, we plot the group-level single voxel autocorrelation maps for each lag, averaged across runs and participants. **C) Autocorrelation clustering (hypothetical values).** The autocorrelation values for each lag were stored in a vector (single voxel autocorrelation vector). The voxels in the ROI were clustered based on the similarity (ED) of single voxel autocorrelation vectors. Single voxel autocorrelation vectors were clustered according to their ED (Blondel et al. 2008). Clustering was performed at the individual-level and at the group-level. **D) Three alternative autocorrelation gradient predictions.** One possibility is that autocorrelation gradients in the hippocampus and ERC would follow the pattern of reciprocal connectivity extending along the anterior–posterior extent. The second possibility is that autocorrelation gradients are driven by physiological or hemodynamic factors. If this were the case, autocorrelation values in the entorhinal cortex should be similar to those in the anterior portion of the hippocampus due to spatial proximity and similar anterior–posterior extent. The third possibility is that autocorrelation values in these structures result from intrinsic functional properties, which could give rise to differentiable patterns in hippocampus and ERC.

patterns (Fig. 1D). The first possibility is that reciprocal connectivity between the hippocampus and ERC along the anterior–posterior axes drives the autocorrelation gradient. If this were the case, we would expect hippocampal and entorhinal gradients to follow an anterior–posterior organization. This would result in similar autocorrelation values in the anterior segments of both regions and similar autocorrelation values in the posterior segments of both regions. A second possibility is that autocorrelation gradients are primarily driven by physiological or hemodynamic factors that differ along the anterior–posterior and superior–inferior dimensions in the brain. In this scenario, autocorrelation values in the entorhinal cortex should be similar to those in the anterior hippocampus as it lies inferior to and extends slightly anterior to the hippocampus. The third—and most interesting—possibility is that the observed gradients reflect differences in the intrinsic organization and processing timescales of these regions, by way of their functional contributions to cognition. For example, the human posterior hippocampus represents local spatial details

(Doeller et al. 2008; Hirshhorn et al. 2012; Lee et al. 2012; Evensmoen et al. 2013) and the anterolateral ERC is important for precise temporal and object processing (Yeung et al. 2017; Bellmund et al. 2019; Montchal et al. 2019); therefore, these regions might exhibit low autocorrelation, which would be representative of a neural signal that is updating more quickly. We might also find that regions such as the anterior hippocampus, which has been shown to represent coarse-grained information (Poppenk et al. 2013), will exhibit high autocorrelation, which would be representative of a neural signal that is changing more slowly. In this case, autocorrelation patterns between the hippocampus and ERC would be differentiable and related to behavior. Further support for this prediction comes from research examining the role of the hippocampal-entorhinal circuit in spatial memory in rodents (Sasaki et al. 2015). This work suggests that the hippocampus has spatial processing that is independent of the inputs from medial entorhinal cortex. Altogether, evidence from humans and rodents supports the prediction that we might observe distinct and opposing gradients in the hippocampus and entorhinal cortex that is driven by differences in mnemonic processes in these regions.

In support of the notion that autocorrelation gradients are driven by intrinsic functional properties of the different brain regions, we found clear evidence of differentiable autocorrelation patterns in hippocampus and ERC, and that hippocampal autocorrelation gradients were meaningfully related to behavior such that increases in navigation difficulty were associated with increases in autocorrelation in the anterior-medial hippocampus. These results are consistent with recent findings from resting-state MRI (Vos de Wael et al. 2018) and a meta-analytic framework (Genon et al. 2021) that suggest that there are two primary connectivity gradients in the hippocampus (one along the anterior–posterior axis and one along the medial-lateral axis). Importantly, we critically extend this work by showing that these gradients are related to behavior. Our single voxel autocorrelation approach yields consistent and precise gradients of single voxel autocorrelation in the hippocampus and ERC, providing a powerful new continuous and data-driven method that can illuminate how temporal dynamics in brain signals relate to complex cognition.

Dataset 1: Resting state fMRI
Materials and methods
Participants

We analyzed resting state fMRI data from 44 participants (14 male) from the HCP Retest dataset. This dataset consists of data from 44 participants who were scanned twice using the full HCP imaging protocol. All subject recruitment procedures and informed consent forms, including consent to share de-identified data, were approved by the Washington University Institutional Review Board (Glasser et al. 2016). The present analysis of this dataset was approved by the University of Toronto research ethics board.

Scanning parameters and preprocessing

Resting state data were collected on a 3T scanner using a multi-band EPI pulse sequence (TR = 720 ms, TE = 33.1 ms, 72 slices with 2-mm thickness, FOV = 208 × 180 mm, voxel size = 2 × 2 mm, Flip angle = 52, Multiband factor = 8, Scan time = 14 min and 33 s). Each run was repeated twice, with a left-to-right and a right-to-left phase encoding direction. To ensure that the results were not due to distortions caused by differences in phase encoding direction, we computed the single voxel autocorrelation and

conducted the autocorrelation clustering on both the left-to-right and the right-to-left phase encoding direction datasets (see Supplementary Fig. S3 for right-to-left phase encoding direction results). The findings for left-to-right and the right-to-left phase encoding direction were similar suggesting that our results are not affected by distortions caused by differences in phase encoding direction. The following results are generated from data with the left-to-right phase encoding direction.

Initial fMRI preprocessing steps already applied to the downloaded data included gradient distortion correction, motion correction (based on FLIRT), field map distortion correction, brain extraction, registration to T_1-weighted image and MNI standard space, intensity normalization, and bias field removal (Glasser et al. 2013; Smith et al. 2013; Van Essen et al. 2013). The data were further preprocessed by running ICA using FSL's MELODIC function with automatic dimensionality estimation limited to a maximum of 250. ICA is able to separate multiple signal and noise components, including head motion and physiological signals. These components are fed into the FIX in FSL (Griffanti et al. 2014; Salimi-Khorshidi et al. 2014), which classifies components into "good" vs. "bad." Bad components are then removed from the data in a "nonaggressive" manner, in which only the unique variance associated with the bad components is removed from the data. Twenty-four confound timeseries derived from the motion estimation (the 6 rigid-body parameter timeseries, their backwards-looking temporal derivatives, plus all 12 resulting regressors squared) are also regressed out. No spatial smoothing was applied; however, there is a degree of smoothing that occurs during the data interpolation which is required for registration of the fMRI data into the standard MNI space. To eliminate high-frequency noise and artifacts, fMRI signals are low-pass filtered using MATLAB IIR Butterworth filter (designfilt function in Signal Processing Toolbox) with a cutoff frequency of 0.1 Hz.

Single voxel autocorrelation method
Computing single voxel autocorrelation

Bilateral hippocampal and entorhinal masks were generated using the Harvard-Oxford Atlas in FSL (see Supplemental Materials for sample BOLD images with outlined hippocampal and entorhinal masks; Supplementary Fig. S4). For each voxel inside each of the ROIs, unbiased autocorrelation (as implemented in MATLAB xcorr function) was calculated. Specifically, the timecourse of a single voxel's activity was correlated with itself shifted by a temporal lag, the length of 1 TR (Dataset 1 TR = 720 ms). We repeated this process, shifting the timecourse forward by 1 lag (720 ms) and correlating it with the original, nonshifted timecourse until a maximum temporal shift of 3,600 ms was reached. We chose 3,600 ms because it has been shown that the autocorrelation of the fMRI signal in the gray matter drops off after approximately 4,000 ms (or 4 s) (i.e. it is not distinguishable from the autocorrelation of other noise) (Bollmann et al. 2018). With a TR of 720 ms, the closest we could get to 4,000 ms without going over was 3,600 ms (or 5 lags). For example, the nonshifted timecourse was correlated with lag 1 (length of 1 TR), lag 2 (length of 2 TRs), etc. (Fig. 1A). The autocorrelation (AC) computed for each lag was stored in a vector. The autocorrelation vector (single voxel autocorrelation vector) contained 5 values (one single voxel autocorrelation for each lag). This approach resulted in a single voxel autocorrelation vector for each voxel. All single voxel autocorrelation values were normalized by subtracting the mean and dividing by the standard deviation within each mask so that meaningful comparisons could be made between the 2 fMRI datasets (resting state and task). Single voxel

autocorrelation maps were then averaged across the first and second runs from the 44 participants to generate an average overall map for visualization purposes (e.g. Fig. 1B). Statistical analyses were conducted on the single voxel autocorrelation for each scanned run. The single voxel autocorrelation generator and autocorrelation cluster generator scripts are available online: https://github.com/aligoles/SingleVoxelAutocorrelation

Single voxel autocorrelation—reliability analysis

To verify that the observed single voxel autocorrelation pattern was not a measurement artifact (e.g. head motion, magnetic field inhomogeneity, physiological artifacts, etc.), we tested the reliability of the single voxel autocorrelation pattern within an individual. In our case, the single voxel autocorrelation pattern was deemed reliable if there was a high degree of agreement between the single voxel autocorrelation values generated from different runs from the same participant compared with runs from different participants. Reliability of the single voxel autocorrelation values was measured by calculating the Euclidean distance (ED) between the single voxel autocorrelation vectors for all pairs of run-wise datasets, and 44 participants with 2 repeated sessions produced 44 intrasubject and 3,784 intersubject ED values. The lower the ED between two single voxel autocorrelation vectors, the higher the similarity between them. We expected to see more similar single voxel autocorrelation patterns between single voxel autocorrelation vectors generated from two runs of the same participant compared with two runs from different participants (lower intrasubject ED compared with intersubject ED). The intersubject and intrasubject ED are not completely independent from one another; therefore, we used nonparametric permutation to test for significance. We randomly shuffled the intra- and intersubject labels and pulled two samples of size 44 (intrasubject) and 3,784 (intersubject). We calculated the mean difference between the 2 samples and repeated this process 10,000 times, resulting in a histogram of mean differences under the null hypothesis (i.e. the difference between intra- and intersubject ED equal to zero). We compared the observed difference between intra- and intersubject EDs with the null distribution and calculated nonparametric *P*-values. Permutation tests were conducted using a permutation testing package in Matlab (Laurens 2021).

Computing single voxel autocorrelation clusters (autocorrelation clustering)

The ED between the single voxel autocorrelation vectors of each voxel pair in each mask was calculated to create a distance matrix. The distance matrix was first normalized (i.e. divided by the maximum value) and then subtracted from 1 to generate a similarity matrix ranging from 0 to 1. This similarity matrix was used to generate hippocampal clusters by applying a Louvain clustering method using the modularity optimization algorithm (Blondel et al. 2008; Wickramaarachchi et al. 2014). Unlike the majority of the clustering methods, modularity optimization does not require to assign the number of clusters and estimates the optimum number of clusters from data. Furthermore, it has been shown that the clustering algorithms, similar to the one we used, generate stable results as long as the sample size is larger than 20 samples per cluster (Dalmaijer et al. 2022). In our study, each ROI mask (whole entorhinal left/right and whole hippocampus left/right) is large enough to generate at least 20 voxels per cluster (see Supplementary Table S2 for full summary of mask sizes). In addition to clustering at the level of each individual run, group-level clustering was performed by averaging the similarity matrices of all participants (for a theoretical schematic, see Fig. 1C).

Autocorrelation clustering—reliability analysis

To better understand the functional subunits of the hippocampus (and ERC), we tested whether the single voxel autocorrelation estimates could be divided into spatially reliable clusters. Reliability of the clustering was measured by calculating the overlap between the generated clusters from each scanned run using the Jaccard coefficient. The Jaccard coefficient of regions A and B is defined as

$$J(A, B) = \frac{|A \cap B|}{|A \cup B|}$$

where $|A \cap B|$ is the number of common voxels in both A and B (intersection) and $|A \cup B|$ is the number of voxels in A and B combined (union). Individual parcellations were then compared with the group-level parcellation to examine the consistency of parcellation. The Jaccard coefficient was calculated both intrasubject (overlap between clusters extracted from two runs from the nth subject) and intersubject (overlap between the cluster from the nth subject and the same cluster estimated in all other subjects).

Assuming that the single voxel autocorrelation pattern is consistent across the two runs of the same participant, we expected there to be greater spatial overlap (higher Jaccard coefficient) among clusters within an individual compared with between different individuals. The Jaccard coefficients for clusters within participants are not completely independent from the Jaccard coefficients for clusters between participants; therefore, we used nonparametric permutation to test for significance. For each cluster, we randomly shuffled the intra- and intersubject labels and pulled two samples of size 44 (intrasubject) and 3,784 (intersubject). We calculated the mean difference between the 2 samples and repeated this process 10,000 times, resulting in a histogram of the mean differences under the null hypothesis (i.e. the difference between intra- and intersubject Jaccard coefficient equal to zero). We compared the observed difference between intra- and intersubject Jaccard coefficients with the null distribution and calculated nonparametric *P*-values.

Temporal SNR control analysis

Temporal signal-to-noise ratio (temporal SNR) is a measure of noise that may interfere with the estimation of the autocorrelation of the fMRI signal and varies in intensity throughout the brain (Hutton et al. 2011). To control for the effects of temporal SNR, we calculated the temporal SNR for each cluster and tested whether the variability in hippocampal autocorrelation could be explained by temporal SNR. We computed the temporal SNR for each voxel by taking the average of the voxel's timecourse and dividing it by the standard deviation. To get the most accurate estimate of the tSNR for each voxel, we used the data that did not have temporal filtering applied. We averaged the temporal SNR across all the voxels in each cluster to get the average temporal SNR per cluster. A table of the average temporal SNR per cluster can be found in Supplementary Table S6. We then conducted linear mixed effects models predicting average autocorrelation of each cluster (lag 1) with Hemisphere (left, right), Cluster (1, 2, 3), and average temporal SNR as fixed effects and participant as the random intercept in the random effects term.
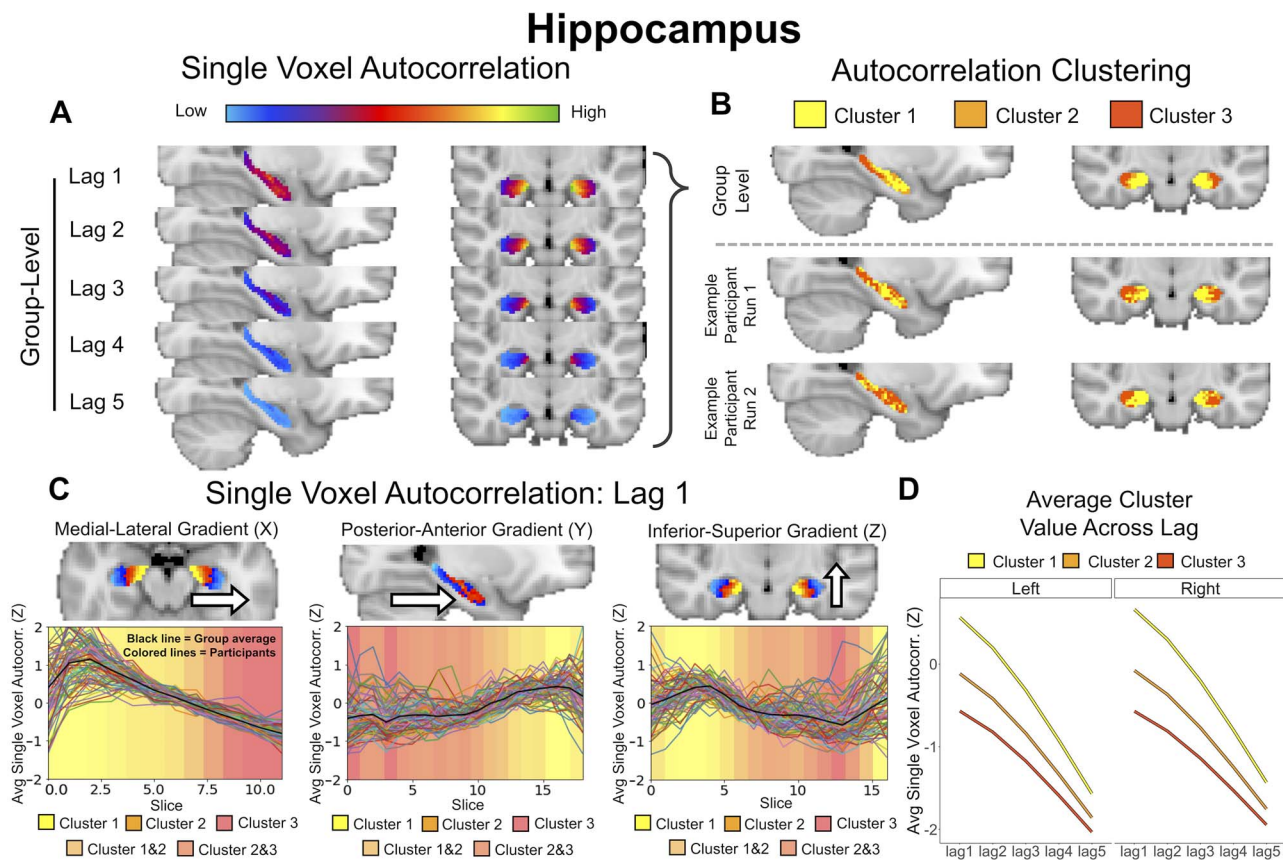
Hippocampus

Fig. 2. Hippocampus. A) Single Voxel Autocorrelation. Group-level single voxel autocorrelation maps averaged across all runs for all participants. **B) Autocorrelation Clustering.** Group-level clusters (top) and run-level cluster maps for two runs from an example participant (bottom). Three distinct clusters were found at both the group and the individual run-level. Cluster 1 was located in the anterior-medial hippocampus, Cluster 3 was located in the posterior-lateral hippocampus, and Cluster 2 was located between Cluster 1 and 3. **C) Single Voxel Autocorrelation: Lag 1.** Single voxel autocorrelation (lag 1) averaged per slice and projected into three axes (*X*, *Y*, and *Z*) to visualize changes in medial-lateral, anterior–posterior, and inferior–superior directions (plots depict left hemisphere; right hemisphere looked similar). The average cluster assignment of voxels on each slice is presented as the background color to show the gradation in values along the three axes. **D) Average Cluster Value Across Lag.** Average group-level single voxel autocorrelation values for each cluster at each lag. Cluster 1 was associated with the highest single voxel autocorrelation values, Cluster 2 with intermediate values, and Cluster 3 with the lowest. This was consistent across all 5 lags.

Results

Hippocampus

Spatial distribution of single voxel autocorrelation

Our analysis correlated the timecourse of activity of each voxel in the hippocampus with activity in that same voxel shifted by a temporal lag of 1 TR, repeating this process until a maximum temporal shift of 5 lags was reached (Fig. 1A) and generated maps of single voxel autocorrelation values for each lag (for a theoretical schematic, see Fig. 1B). We found that single voxel autocorrelation maps at the group level (lags 1–5) showed a notable difference in the distribution of single voxel autocorrelation values along hippocampal axes (Fig. 2A). More specifically, voxels with higher single voxel autocorrelation were mainly in the anterior-medial region, whereas voxels with lower single voxel autocorrelation were mainly in the posterior-lateral region (in both left and right hippocampus). As shown in Fig. 2A, although the overall autocorrelation decreased as the lag increased, the overall pattern of autocorrelation gradients was similar for lags 1–5.

Single voxel autocorrelation—reliability results

We next tested the reliability of these results. Here, we defined a reliable result as one in which single voxel autocorrelation

vectors generated from two runs of the *same* participant were more similar than two runs from *different* participants (lower intrasubject EDs compared with intersubject EDs). Nonparametric permutation tests comparing intrasubject and intersubject ED revealed reliable results in both the left (intrasubject mean ± SD: 7.43 ± 2.07, intersubject mean ± SD: 9.38 ± 2.22, $P < 0.0001$) and right hippocampus (intrasubject mean ± SD: 7.22 ± 1.98, intersubject mean ± SD: 9.02 ± 2.02, $P < 0.0001$) (Supplementary Fig. S1A). These high intrasubject similarity values suggest that the single voxel autocorrelation pattern is an intrinsic feature of the brain, likely originating from neuronal sources, rather than noise or imaging artifacts.

Autocorrelation clustering

Data-driven clustering of the single voxel autocorrelation vectors revealed three distinct clusters in both the left and right hippocampus (Fig. 2B); notably, past work that segmented the hippocampus into 2 ROIs (anterior and posterior) a priori would not have been able to detect the presence of this third cluster. Consistently across all 5 lags, we found that Cluster 1 had the highest single voxel autocorrelation values and was located in the anterior-medial hippocampus (Fig. 2D). Cluster 3 had the lowest single voxel autocorrelation values and was located in

the posterior-lateral part of the hippocampus. Cluster 2 had intermediate single voxel autocorrelation values and was located between Clusters 1 and 3. These three clusters were also reliably observed at the individual level (cluster maps from two runs of an example participant are shown in Fig. 2B). Cluster 1 was the largest cluster, followed by Cluster 3 and Cluster 2. Cluster 2 was the smallest cluster. For a summary of the number of voxels within each cluster, see Supplementary Table S3.

In summary, clustering revealed a high-to-low single voxel autocorrelation gradient along the anterior–posterior axis, consistent with what has been previously found in the literature (Brunec, Bellana, et al. 2018; Raut et al. 2020). In addition, we found differences along the medial-lateral axis, as well as a prominent anterior-medial cluster of high single voxel autocorrelation that could be distinguished from a posterior-lateral cluster of low single voxel autocorrelation. While previous methods using predetermined anterior/posterior ROI masks might have missed this medial-lateral distinction, our data-driven method provides evidence that an autocorrelation gradient exists along multiple spatial dimensions.

Autocorrelation clustering—reliability results

The reliability of single voxel autocorrelation clustering was evaluated by measuring spatial overlap between clusters, calculated by the Jaccard coefficient (Supplementary Fig. S1B). Here, we defined a reliable result as one in which the spatial distribution of autocorrelation clusters was consistent across the 2 runs of the same participant, indicated by greater overlap (higher Jaccard coefficient) among clusters *within* an individual compared with *between* different individuals. Using nonparametric permutation, we found high reliability for clusters in the bilateral hippocampus, specifically Cluster 1 (Left: $P < 0.001$; Right: $P < 0.001$) and Cluster 3 (Left: $P < 0.001$; Right: $P < 0.001$). These findings of high intra- and intersubject overlap suggest that Clusters 1 and 3 were highly reliable, within individuals. Cluster 2, however, had significantly lower overlap (Left: $P = 0.06$; Right: $P = 0.007$), suggesting more variability within individuals.

Temporal SNR control analysis

To rule out the possibility that the hippocampal autocorrelation clusters are being driven by noise, we calculated the temporal SNR for each cluster and tested whether the hippocampal autocorrelation could be explained by temporal SNR. We ran a linear mixed effects model with Hemisphere (left, right), Cluster (1, 2, 3), and temporal SNR as fixed effects predictors and average autocorrelation of each cluster (lag 1) as the predicted variable. We found a significant effect of Cluster ($F(2,461.84) = 6619.86$, $P < 0.001$), suggesting that even when temporal SNR is included in the model, clusters significantly explained the variance of the autocorrelation. We did not find a significant effect of temporal SNR. Additionally, we ran another model without Cluster as a fixed effect predictor and compared the two models (the one with and without Cluster) using a Chi square test. We found that the model including Cluster was significant $\chi^2(8, n = 19) = 1,422.9$, $P < 0.001$, indicating that the model including Cluster was a better fit of the data compared with the model that only had hemisphere and temporal SNR alone. Together these results suggest that temporal SNR alone cannot explain the hippocampal autocorrelation clusters.

Gradients of single voxel autocorrelation (lag 1)

The single voxel autocorrelation and autocorrelation clustering results presented above both suggest the presence of an autocorrelation gradient along 2 main axes: the anterior–posterior axis and the medial-lateral axis. To examine these individual gradients more precisely, we plotted the single voxel autocorrelation across hippocampal slices along the *X* (medial-lateral), *Y* (posterior–anterior), and *Z* (inferior–superior) axes. We observed consistent gradients in every participant. Specifically, single voxel autocorrelation gradually decreased in the medial-to-lateral direction and increased in the posterior-to-anterior direction (Fig. 2C; we focused on lag 1, but a similar pattern was revealed across all lags, as shown in Fig. 2A). A rough gradient of high-to-low autocorrelation was also observed in the inferior–superior axis, which is due to the angle of the hippocampus (i.e. the anterior hippocampus is located more inferiorly relative to the posterior hippocampus). The medial-lateral gradient in the hippocampus was not expected; therefore, we wanted to rule out the possibility that this was observed by chance. To do this, we first fit a line to each individual's autocorrelation data in the medial-lateral axis (i.e. the colored lines in Fig. 2C, left). We computed the slope of the line for each individual run. Note, each individual in Dataset 1 had two scanned runs. We computed the slope for each run separately and then averaged the two runs to get one average slope for each individual. We compared the distribution of slopes to zero by conducting a one sample *t*-test on the average slopes to determine whether they were significantly greater than zero. We did this for each hemisphere separately. We found that average medial-lateral slopes in both the left and right hemisphere were significantly greater than zero (Left hemisphere: $t(43) = 17.34$, $P < 0.001$; Right hemisphere: $t(43) = 42.92$, $P < 0.001$). These results suggest that the medial-lateral gradient in the hippocampus was not due to chance (see Supplementary Fig. S2 and Supplementary Table S1 for a full summary of the slopes and *t*-test results).

When we investigated the spatial distribution of the 3 clusters (projected on the background of the plots in Fig. 2C), we observed a gradient of cluster assignment that complemented the single voxel autocorrelation gradients. Specifically, high-to-low single voxel autocorrelation gradients were also associated with a cluster gradient from Cluster 1 to Cluster 3.

Entorhinal cortex
Spatial distribution of single voxel autocorrelation

We repeated the analyses above in the ERC. To illustrate the distribution of autocorrelation values of individual voxels throughout the ERC, we plotted the group-level single voxel autocorrelation maps for lags 1–5 (Fig. 3A). The maps illustrate a difference in single voxel autocorrelation throughout the ERC. Specifically, voxels with higher single voxel autocorrelation were mainly in the posterior-medial region, whereas voxels with lower single voxel autocorrelation were mainly in the anterior-lateral region (in both left and right ERC).

Single voxel autocorrelation—reliability results

Nonparametric permutation tests comparing intrasubject and intersubject ED revealed reliable results in both the left (intrasubject mean ± SD: 11.43 ± 3.64, intersubject mean ± SD: 12.87 ± 2.83, $P < 0.001$ and right ERC (intrasubject mean ± SD: 10.41 ± 2.63, intersubject mean ± SD: 13.19 ± 2.53, $P < 0.001$; see Supplementary Fig. S1C). This analysis demonstrates the reliability of the single voxel autocorrelation and suggests that single voxel autocorrelation patterns between vectors generated from two runs of the *same* participant were more similar than two runs from *different* participants (lower intrasubject EDs compared with intersubject EDs).
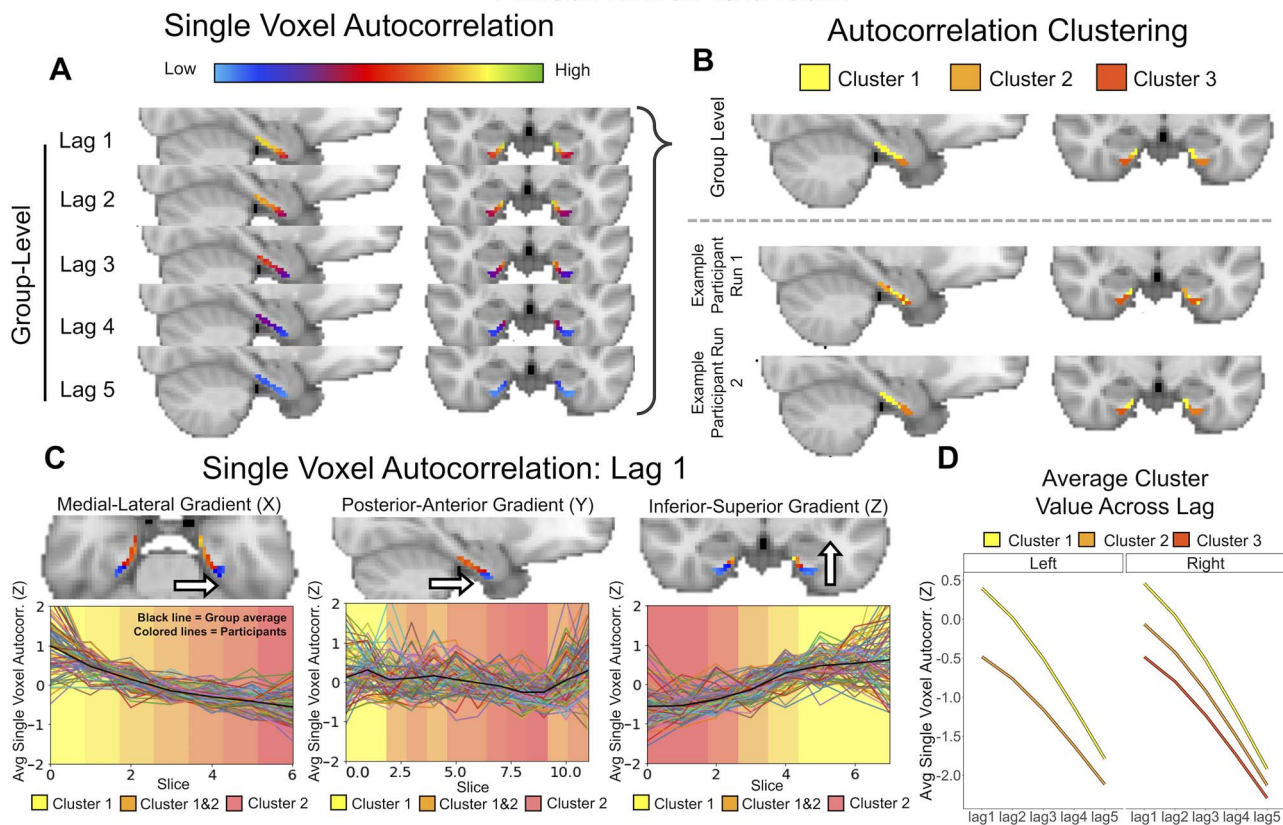
Entorhinal Cortex

Fig. 3. Entorhinal cortex. A) Single Voxel Autocorrelation. Group-level single voxel autocorrelation maps averaged across all runs for all participants. **B) Autocorrelation Clustering.** Group-level clusters (top) and run-level cluster maps for two runs from an example participant (bottom). Two distinct clusters were found in the left hemisphere and three in the right hemisphere. In the left hemisphere, Cluster 1 was located in the posterior-medial ERC and Cluster 2 was in the anterior-lateral ERC. In the right hemisphere, Cluster 1 was located in the posterior-medial ERC, Cluster 3 was located in the anterior-lateral ERC, and Cluster 2 was located between Cluster 1 and 3. **C) Single Voxel Autocorrelation: Lag 1.** Single voxel autocorrelation projected below onto three axes (*X*, *Y*, and *Z*) to visualize changes in medial-lateral, anterior–posterior, and inferior–superior directions (for the left hemisphere; right hemisphere looked similar). The average cluster assignment of voxels on each slice is presented as the background color to show the gradation in values along the three axes (Note the gradation depicts only Cluster 1 and 2 as there were only two significant clusters found in the left hemisphere). **D) Average Cluster Value Across Lag.** Average group-level single voxel autocorrelation values for each cluster at each lag. In the left hemisphere, Cluster 1 was associated with the highest single voxel autocorrelation values and Cluster 2 with low autocorrelation values. In the right hemisphere, Cluster 1 was associated with the highest single voxel autocorrelation, Cluster 2 with intermediate values, and Cluster 3 with the lowest. This was consistent across all 5 lags.

Autocorrelation clustering

The group-level clustering analysis on the voxels within the ERC revealed two distinct clusters in the left hemisphere and three clusters in the right (Fig. 3B). For comparison, cluster maps from two runs of an example participant are shown in Fig. 3B. Cluster 1 was located in the posteromedial ERC and had the highest single voxel autocorrelation values in both left and right hemispheres. Cluster 2 was observed in the left hemisphere and was located toward the anterior-lateral ERC with low single voxel autocorrelation values. In the right hemisphere, it was an intermediate cluster. Cluster 3 was only observed consistently in the right hemisphere and was located in the anterior-lateral ERC with the lowest single voxel autocorrelation values. We computed the group-level single voxel autocorrelation for each cluster and plotted it across all 5 lags (Fig. 3D). Across all 5 lags, Cluster 1 consistently had the highest single voxel autocorrelation values, followed by Cluster 2 and Cluster 3. In the right hemisphere, Cluster 1 was the largest cluster, followed by Cluster 3 and Cluster 2. In the left hemisphere, Cluster 1 was the largest cluster and Cluster 2 was the smallest cluster. For a summary of the number of voxels within each cluster, see Supplementary Table S3.

Autocorrelation clustering—reliability results

The reliability measure for ERC clusters was calculated by the Jaccard coefficient Supplementary Fig. S1D. Nonparametric permutation tests comparing intrasubject and intersubject cluster overlap revealed reliable results in the left and right hemisphere. In the left hemisphere, the Cluster 1 ($P < 0.001$) and Cluster 2 ($P < 0.001$) were reliable. In the right hemisphere, Cluster 1 ($P < 0.001$) and Cluster 3 ($P < 0.001$) were reliable. This suggests that these clusters were highly reliable within individuals. In the right hemisphere, Cluster 2 had very small Jaccard values, suggesting less reliability within individuals (Right: $P = 0.53$).

Temporal SNR control analysis

We calculated the temporal SNR for each cluster and tested whether the entorhinal autocorrelation clusters could be explained by temporal SNR. We ran a linear mixed effects model with Hemisphere (left, right), Cluster (1, 2, 3), and temporal SNR as fixed effects predictors and average autocorrelation of each cluster (lag 1) as the predicted variable. We found a significant effect of Cluster ($F(2,396.42) = 1,237.65$, $P < 0.001$), suggesting that even when temporal SNR is included in the model, clusters

significantly explained the variance in the autocorrelation. We did not find a significant effect of temporal SNR. Additionally, we ran another model without Cluster as a fixed effect predictor and compared the two models (the one with and without Cluster) using a Chi square test. We found that the model including Cluster was significant χ^2 (8, $n = 19$) = 781.62, $P < 0.001$, indicating that the model including Cluster was a better fit of the data compared with the model that only had hemisphere and temporal SNR alone. Altogether, these results suggest that temporal SNR alone cannot explain the entorhinal autocorrelation clusters.

Gradients of single voxel autocorrelation (lag 1)

Single voxel autocorrelation values for lag 1 were projected onto *X* (medial-lateral), *Y* (posterior–anterior), and *Z* (inferior–superior) axes. As shown in Fig. 3C, in every participant, single voxel autocorrelation values gradually decreased in the medial-to-lateral direction and the posterior-to-anterior direction (Fig. 3C). We found a gradient of low-to-high autocorrelation along the inferior–superior axis, which is due to the fact that the posterior region of the ERC is more superior than its anterior region. We observed a gradient of cluster assignment that complemented the single voxel autocorrelation gradients, where high-to-low gradients were also associated with a cluster gradient from Cluster1 to Cluster 2.

Dataset 2: Navigation fMRI

We next aimed to replicate the observed effects in task fMRI and relate changes in single voxel autocorrelation to behavior. Specifically, we were interested in how single voxel autocorrelation throughout the hippocampal long axis might be modulated by differences in difficulty during a temporally extended navigation task. Therefore, we performed our single voxel autocorrelation analyses on a task fMRI dataset acquired, while participants navigated in a familiar virtual reality environment (previously described in Brunec, Bellana, et al. 2018). Due to the lower spatial resolution in this dataset, we were not able to examine the ERC and, thus, these analyses focused only on the hippocampus (see Supplemental Materials for sample BOLD images illustrating the poor resolution of the entorhinal cortex in Dataset 2; Supplementary Fig. S4).

Material and methods
Participants

Nineteen participants (9 males; mean age 22.58 years, range 19–30 years) were scanned while navigating Google Street View routes around the city of Toronto. All subject recruitment procedures and informed consent was approved by the University of Toronto research ethics board.

Paradigm

Participants met with the experimenter ahead of time and built routes that were either highly familiar or less familiar to them (e.g. frequently traveled or not). Participants then returned to the lab for their second session and were scanned, while they navigated four different types of routes. (i) Familiar: participants started at a familiar landmark and navigated to a familiar goal destination via a familiar route, (ii) Mirrored: participants started at a familiar landmark and traveled to a familiar destination via a familiar route, but the images of the route were mirrored (left–right reversed), (iii) Unfamiliar: participants started at a familiar location, navigated to a familiar destination, but they were instructed to take an unfamiliar route between the two, and (iv) GPS: participants started at an unfamiliar location in

an unfamiliar part of town and followed the directions displayed by an arrow on the screen to the goal destination. Participants completed 4 unique routes in each condition, 16 routes in total (1 route = 1 scanned run). At the end of each route, participants rated the difficulty of the route on a scale from 1 (difficult) to 9 (easy).

Scanning parameters and preprocessing

Participants were scanned with a 3T Siemens MRI scanner at Baycrest's Rotman Research Institute. A high-resolution 3D MPRAGE T_1-weighted pulse sequence image (160 axial slices, 1-mm thick, FOV = 256 mm) was first obtained to register functional maps against brain anatomy. Functional imaging was performed to measure brain activation by means of the blood oxygenation level dependent (BOLD) effect. Functional T_2*-weighted images were acquired using echo-planar imaging (30 axial slices, 5-mm thick, TR = 2,000 ms, TE = 30 ms, flip angle = 70°, FOV = 200 mm). The native EPI resolution was 64×64 with a voxel size of 3.5 mm × 3.5 mm × 5.0 mm. Images were first corrected for head motion using the Analysis of Functional NeuroImages (AFNI; Cox 1996). All subsequent analysis steps were conducted using the statistical parametric mapping software SPM12.

Preprocessing involved slice timing correction, spatial realignment and co-registration, with a resampled voxel size of 3-mm isotropic, with no spatial smoothing. As all of our analyses rely on covariance, we additionally regressed out the mean time-courses from participant-specific white matter, and cerebrospinal fluid masks, alongside estimates of the 6 rigid body motion parameters from each EPI run. To further correct for the effects of motion which may persist despite standard processing (Power et al. 2012), an additional motion scrubbing procedure was added to the end of our preprocessing pipeline. Outlier timepoints were identified using the conservative multivariate technique from Campbell et al. (2013), which involves using Principal Components Analysis (PCA) to calculate the displacement of timepoints relative to surrounding timepoints. The displacement values were then compared with a Gamma probability distribution and timepoints that were identified at $P < 0.05$ were labeled as motion outliers. The time points that were motion outliers in both the 6 rigid-body motion parameter estimates and BOLD signal were removed, and outlying BOLD signal was replaced by interpolating across neighboring data points. This motion scrubbing approach further minimizes any effects of motion-induced spikes on the BOLD signal, over and beyond standard motion regression, without leaving sharp discontinuities due to the removal of outlier volumes (for details, see Campbell et al. 2013). To enable comparisons at the group-level, the final step of the preprocessing involved warping participants' functional data to the MNI-space template.

Single voxel autocorrelation method
Computing single voxel autocorrelation

To compute the single voxel autocorrelation, we completed the same procedure outlined in Dataset 1. We used resampled the bilateral hippocampal mask from Dataset 1 to 3 mm in order to extract the HPC voxels in Dataset 2 (see Supplemental Materials for sample BOLD images with outlined hippocampal mask; Supplementary Fig. S4). For each voxel, the single voxel autocorrelation was calculated by repeatedly shifting temporal lags (length of 1 TR) until a maximum lag of 4 s was reached. In Dataset 2, the TR was 2,000 ms; therefore, single voxel autocorrelation for 2 lags (or 2 TRs) was calculated, resulting in a maximum lag of 4 s. As outlined in the procedure above, single voxel autocorrelation values were normalized by subtracting the mean and dividing by

the standard deviation. Single voxel autocorrelation was calculated for all four runs of each navigational condition (Familiar, Unfamiliar, Mirrored, GPS). The single voxel autocorrelation was averaged across the four scanned runs (unique routes), resulting in four different maps (one for each navigational condition). Single voxel autocorrelation maps were then averaged across the 19 participants to generate an average group map for each navigation condition.

Participants completed 16 navigation runs (four in each condition) at their own pace. Because the conditions varied in difficulty, the average number of TRs differed across conditions and participants. Every route was 2–10 km long and the average run (route) length was 137.6 TRs (2 s TRs). The average number of TRs was lowest in the GPS condition ($M = 92.13$, $SD = 17.44$), followed by the Familiar condition ($M = 136.45$, $SD = 39.18$), the Mirrored condition ($M = 155.73$, $SD = 36.84$), and the Unfamiliar condition ($M = 158.78$, $SD = 32.13$). In order to compare single voxel autocorrelation across scanned runs with a similar number of TRs/lengths, we chose to filter out any runs that were unusually short (that the participant either did not complete or completed very quickly). We excluded runs that were less than 88 TRs long. This resulted in an average of 13.36 runs ($SD = 1.21$) per participant. The GPS runs were disproportionately shorter than the other conditions, resulting in more GPS runs excluded than other conditions. For two participants, all four control runs were less than 88 TRs long, and therefore, all of their control runs were excluded. The average number of routes included in the following analyses per participant is as follows: Mirrored ($M = 3.89$, $SD = 0.31$), Unfamiliar ($M = 3.84$, $SD = 0.50$), Familiar ($M = 3.68$, $SD = 0.47$), and GPS ($M = 1.95$, $SD = 1.22$).

Computing autocorrelation clusters (autocorrelation clustering)

We repeated the single voxel autocorrelation clustering procedure described above in Dataset 1 to determine clusters of single voxel autocorrelation within each navigational condition. The ED between the single voxel autocorrelation vectors (composed of lag 1 and lag 2) of each voxel pair in each mask was calculated and the Louvain Clustering method was applied to generate the clusters.

Relating single voxel autocorrelation to navigation condition

Comparing average autocorrelation of clusters across navigation condition

To investigate how the spatial distribution of single voxel autocorrelation is related to navigation difficulty, we compared the average single voxel autocorrelation (lag 1 and 2) of each cluster across the four different conditions: GPS, Familiar, Unfamiliar, and Mirrored. We conducted the analysis of lag 1 and lag 2 separately. The results of the lag 1 analysis were very similar to lag 2; therefore, we only present the results for lag 1. A full description of the analysis of lag 2 can be found in Supplementary Fig. S5. For each participant, we averaged the single voxel autocorrelation (lag 1) across all voxels in each cluster and Z transformed the values. To test whether there was a significant difference between single voxel autocorrelation during different navigation conditions, we modeled the data using linear mixed effects models with fixed effects based on experimental hypothesis and random effects structures to account for the effects of individual participants. We included Hemisphere, Cluster, and Navigation condition as fixed effects and participant as the random intercept in the random effects term. We began each model with a random effects structure that was the maximal justified by the design

(including random slopes) (Barr et al. 2013). We systematically pruned the random effects structure until the model converged while avoiding a singular solution (i.e. overfitting) (Singmann and Kellen 2019). Models that included random slopes either failed to converge or reached a singular solution; therefore, the models reported only include random intercepts for random effects term. This analysis was conducted in R (R Core Team 2019) using the afex (Singmann et al. 2020) and the tidyverse packages (Wickham 2017). We used the Tukey method to correct P-values for multiple comparisons in post hoc tests.

Head motion is a noise artifact that may contribute to the autocorrelation signal. This is why, in addition to regressing out the estimates of the 6 rigid body motion parameters from each scan, we conducted an additional motion scrubbing step where we removed time points that were identified as outliers in the 6 rigid body motion parameters and those that were outliers identified using PCA (Campbell et al. 2013). To ensure, however, that the differences in autocorrelation we observed across navigation conditions was not due to differences in head motion across the different conditions, we conducted an additional head motion control analysis (see Supplementary Table S5). We found that differences in head motion across navigation conditions could not account for the differences in autocorrelation observed across navigation condition.

Temporal SNR control analysis

We conducted the control analysis described in Dataset 1 to make sure that the difference in hippocampal autocorrelation across navigation conditions that we observed could not solely be explained by temporal SNR. Here, we calculated the temporal SNR for each cluster for each of the four navigation conditions separately (GPS, Familiar, Unfamiliar, and Mirrored). We ran a linear mixed effects model on the average autocorrelation per cluster (lag 1) with Hemisphere (left, right), Cluster (1, 2, 3), Navigation condition (GPS, Familiar, Unfamiliar, Mirrored), and temporal SNR per cluster as fixed effects predictors.

Results
Hippocampus
Spatial distribution of single voxel autocorrelation

We observed a difference in single voxel autocorrelation along the anterior–posterior and medial-lateral hippocampal axes, where voxels with higher single voxel autocorrelation were found in the anterior-medial hippocampus and voxels with lower single voxel autocorrelation were found in the posterior-lateral hippocampus. Figure 4A shows the group-level single voxel autocorrelation maps for the four navigation conditions (as single voxel autocorrelation maps for lags 1–2 were similar, only lag 1 is depicted in Fig. 4A). The spatial distribution of single voxel autocorrelation was similar across navigation conditions and was also similar to the findings from Dataset 1. We again observed a medial-lateral gradient in the hippocampus. To rule out the possibility that this was observed by chance, we first fit a line to each individual's autocorrelation data in the medial-lateral axis and compared the distribution of slopes to zero. For each individual, we computed the slope for each run and then averaged the slopes in each navigation condition so that each individual had one average slope per navigation condition. We computed one sampled t-tests for each hemisphere separately. All P's < 0.05 suggesting that the medial-lateral slopes in all four navigation conditions in both hemispheres were significantly greater than zero (see Supplementary Fig. S2 and Supplementary Table S1 for
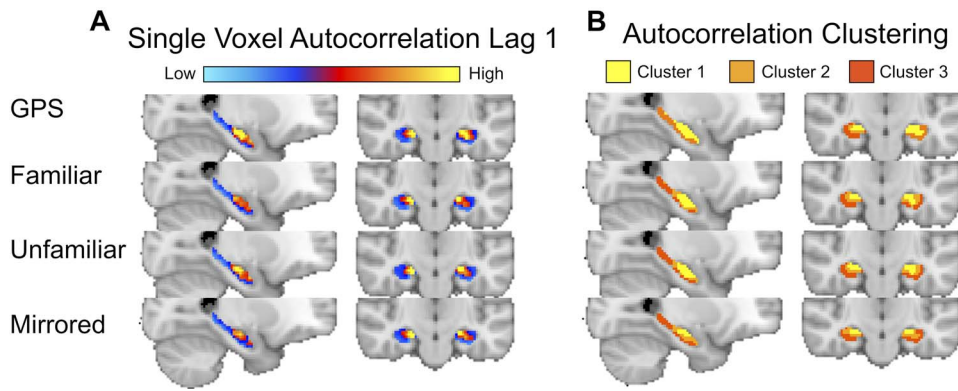
Fig. 4. A) Single Voxel Autocorrelation: Lag 1. Single voxel autocorrelation values at lag 1 for every voxel in the hippocampus during spatial navigation. These values are averaged across run and participant for each of the GPS, Familiar, Unfamiliar, and Mirrored conditions. A gradient from high to low autocorrelation is observed in the anterior–posterior and medial-lateral axes, across all navigation conditions. **B) Autocorrelation Clustering.** Cluster maps averaged across run and participant for each route type. High single voxel autocorrelation voxels cluster in the anterior-medial hippocampus and low single voxel autocorrelation voxels cluster in the posterior-lateral hippocampus.

a full summary of the slopes and *t*-test results). These results suggest that we did not observe the medial-lateral gradient by chance. In the next section, we investigate the differences between navigation conditions in more depth.

Autocorrelation clustering

As with Dataset 1, autocorrelation clustering revealed three distinct clusters in the left and right hemispheres for the Familiar, Unfamiliar, and Mirrored conditions (Fig. 4B). For Familiar, Unfamiliar, and Mirrored conditions, Cluster 1 was located in the anterior-medial HPC and had the highest single voxel autocorrelation. Cluster 3 was located in the posterior-lateral hippocampus and had the lowest single voxel autocorrelation. Cluster 2 was located between Cluster 1 and 3 and had intermediate single voxel autocorrelation. The GPS condition had three clusters in the right hemisphere and only two in the left. The size of the clusters produced in each navigation condition was similar; therefore, we averaged across navigation condition and computed the size (in voxels) of each cluster. Cluster 3 was the largest, followed by Cluster 1 and Cluster 2. Cluster 2 was the smallest cluster. For a summary of the number of voxels within each cluster, see Supplementary Table S3.

Relating single voxel autocorrelation to navigation condition

Subjective difficulty ratings collected after each route (1 = difficult, 9 = easy) suggested that across the navigation conditions, navigational difficulty increased. Participants rated the GPS routes as the easiest ($M = 7.2$, $SD = 1.46$), followed by the Familiar condition ($M = 6.98$, $SD = 2.05$), Unfamiliar condition ($M = 4.35$, $SD = 2.66$), and the Mirrored condition, which was subjectively the most difficult ($M = 3.97$, $SD = 2.42$).

As navigation becomes more difficult, it is beneficial to integrate or maintain information over time, which may be reflected in changes in single voxel autocorrelation. Specifically, more stable neural dynamics might enable individuals to maintain information as one moves towards a goal. This prediction leads to two possibilities. In the first, as navigational difficulty increases, we might observe a uniform change in single voxel autocorrelation across all voxels in the hippocampus. A second possibility is that as difficulty increases, voxels that tend to exhibit high autocorrelation during rest would differentially increase their autocorrelation relative to voxels that tend to exhibit low autocorrelation.

To investigate these possibilities, we calculated the average single voxel autocorrelation (lag 1) of each of the three clusters for each navigation condition.

If navigational difficulty leads to a uniform increase in autocorrelation, we would observe no interaction between cluster and navigation condition. However, if navigational difficulty disproportionately affects the regions of the hippocampus that show high autocorrelation during rest (Fig. 2), then more difficult routes would elicit a larger change in autocorrelation in the anterior-medial cluster (Cluster 1) compared with the more intermediate or posterior-lateral clusters (Clusters 2 and 3).

Comparing average autocorrelation of clusters across navigation condition

We compared the average single voxel autocorrelation of each cluster across the four route conditions: GPS, Familiar, Unfamiliar, and Mirrored. In both the left and right hemisphere, across all four navigation conditions, Cluster 1 had the highest autocorrelation (Left: $M = 1.00$, $SD = 1.27$; Right: $M = 0.77$, $SD = 1.44$) compared with Cluster 2 (Left: $M = -0.11$, $SD = 0.64$; Right: $M = -0.21$, $SD = 0.51$) and Cluster 3 (Left: $M = -0.55$, $SD = 0.11$; Right: $M = -0.55$, $SD = 0.13$), which is consistent with our findings from the autocorrelation clustering in Dataset 1.

To test whether there was a significant difference between single voxel autocorrelation during different navigation conditions, we ran a linear mixed effects model on the autocorrelation of the clusters. We included Hemisphere, Cluster, and Navigation condition (GPS, Familiar, Unfamiliar, and Mirrored) as predictors in the model and participant as a random intercept in the random effects term. We found a significant effect of Hemisphere ($F(1, 1,383.19) = 10.18$, $P < 0.001$), a significant effect of Cluster ($F(2, 1,383.10) = 449.48$, $P < 0.001$), and a significant effect of Navigation condition ($F(3, 1,384.94) = 7.85$, $P < 0.001$) (Fig. 5). We found a significant Cluster × Hemisphere interaction ($F(2, 1,383.18) = 4.49$, $P < 0.05$) and a significant Cluster × Navigation condition interaction ($F(6, 1,383.12) = 5.53$, $P < 0.001$).

A post hoc analysis of the main effect of Hemisphere revealed that the single voxel autocorrelation was greater in the left hippocampus compared with the right hippocampus ($t(1,383) = 3.19$, $P < 0.01$). Pairwise comparisons of the clusters suggest that autocorrelation was greatest in Cluster 1 compared with Cluster 2 ($t(1,383) = 21.01$, $P < 0.001$) and Cluster 3 ($t(1,383) = 29.45$, $P < 0.001$). Cluster 2 was greater than Cluster 3 ($t(1,383) = 8.96$, $P < 0.001$).
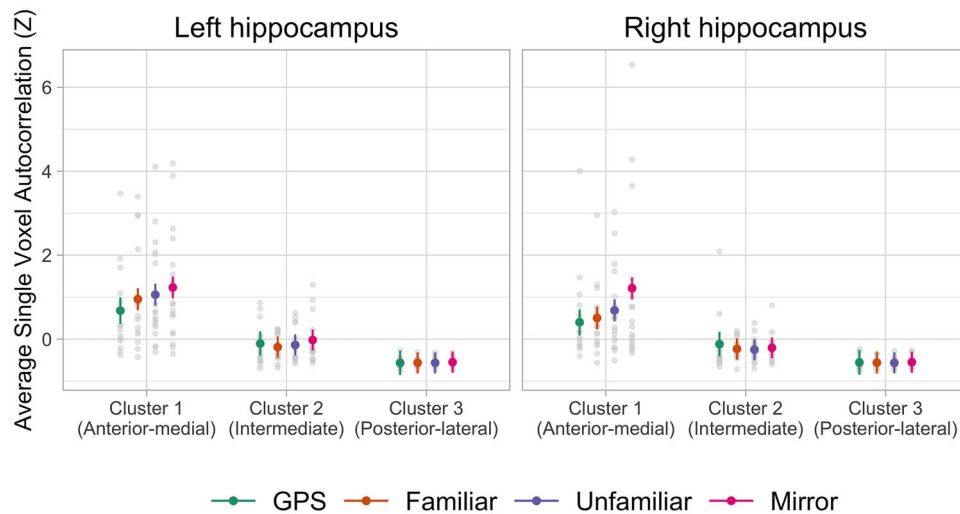
Fig. 5. Effect of navigational condition on average single voxel autocorrelation. Average single voxel autocorrelation (lag 1) per cluster for each navigation condition. Across both hemispheres, Cluster 1 had greater average single voxel autocorrelation compared with Clusters 2 and 3. The average single voxel autocorrelation in Cluster 1 was modulated by navigational condition (in both left and right hemispheres). The autocorrelation of Cluster 1 was greatest when participants navigated Mirrored routes compared with GPS, Familiar, and Unfamiliar routes. The autocorrelation for Unfamiliar routes was greater than GPS routes. There was no significant difference between Unfamiliar and Familiar; however, the Unfamiliar routes were numerically greater than Familiar (in both hemispheres). There was no significant difference between the two easiest routes (Familiar and GPS). Error bars denote standard error.

Analysis of the main effect of Navigation condition (collapsed across Hemisphere and Cluster) revealed that autocorrelation was significantly greater for the Mirrored compared with GPS ($t(1,387) = 3.86$, $P < 0.001$), compared with Familiar ($t(1,383) = 4.14$, $P < 0.001$), and compared with Unfamiliar ($t(1,383) = 3.11$, $P < 0.05$). There was no significant difference between Familiar and Unfamiliar conditions and no significant difference between Familiar and GPS.

An analysis of the Cluster × Hemisphere interaction revealed that differences between hemispheres were driven by differences in Cluster 1, where the left hemisphere was greater than the right ($t(1,383) = 3.93$, $P < 0.001$). There were no significant differences between Cluster 2 and Cluster 3 in the left and right hemispheres. Furthermore, the Navigation condition × Cluster interaction revealed that there were significant differences between navigation conditions, particularly in Cluster 1. There were no significant differences between navigation conditions in Cluster 2 or Cluster 3. Therefore, we report the pairwise comparisons for the different navigation conditions in Cluster 1, collapsed across hemispheres.

In Cluster 1, the routes rated as most difficult, the Mirrored routes, had higher autocorrelation compared with GPS ($t(1,384) = 6.22$, $P < 0.001$), Familiar ($t(1,383) = 5.45$, $P < 0.001$), and Unfamiliar ($t(1,383) = 3.95$, $P < 0.001$). The Unfamiliar routes had higher autocorrelation compared with GPS ($t(1,384) = 3.03$, $P < 0.001$). There was no significant difference between the two easier routes (Familiar and GPS) ($P = 0.33$). There were no significant differences in autocorrelation between Unfamiliar and Familiar ($P = 0.39$); however, Unfamiliar routes were numerically greater than Familiar (in both hemispheres). This finding suggests that more difficult navigation conditions were related to increases in the autocorrelation in the anterior-medial hippocampus (Cluster 1).

Temporal SNR control analysis

We ran a linear mixed effects model on the average autocorrelation per cluster (lag 1) with Hemisphere (left, right), Cluster (1, 2, 3), Navigation condition (GPS, Familiar, Unfamiliar, Mirrored), and temporal SNR per cluster as fixed effects predictors. We found a significant effect of Cluster ($F(2, 1,370.90) = 99.53$, $P < 0.001$), a significant effect of Navigation condition ($F(3, 1,359.73) = 4.74$, $P < 0.01$), and a significant effect of temporal SNR ($F(1, 1,376.58) = 840.80$, $P < 0.001$). Importantly, we found an interaction of Cluster and Navigation condition ($F(6, 1,359.73) = 2.55$, $P < 0.05$). This suggests that Cluster and Navigation condition significantly explained the variance in autocorrelation beyond temporal SNR.

Additionally, we ran two different model comparisons. First, we compared two models with Hemisphere, Navigation condition, and temporal SNR as predictors. One model included Cluster as a predictor and one model did not. We compared the models with a Chi square test and found that the model including Cluster was significant χ^2 (8, $n = 19$) $= 689.47$, $P < 0.001$, indicating that the model including Cluster was a better fit of the data than the model without. Next, we compared two models with Hemisphere, Cluster, and temporal SNR as predictors. One model included Navigation condition as a predictor and one model did not. We compared the models with a Chi square test and found that the model including Navigation condition was significant χ^2 (36, $n = 19$) $= 140.827$, $P < 0.001$, indicating that the model including Navigation condition was a better fit of the data than the model without. These results suggest that temporal SNR alone cannot explain the relationship between autocorrelation and navigation condition.

Discussion

Here, we present a novel autocorrelation measure to investigate intrahippocampal and intra-entorhinal processing. We provide evidence of a medial-lateral gradient of autocorrelation in the hippocampus, as well as a posterior-medial and anterior-lateral gradient in the ERC. We found that voxels in the anterior-medial hippocampus have a highly correlated, slower changing signal, whereas voxels in the posterior-lateral hippocampus have a less

correlated, faster changing signal (Fig. 2) (Brunec, Bellana, et al. 2018; Raut et al. 2020). Our study highlights the importance of examining the medial-lateral axis of the hippocampus, which has previously been an understudied feature of hippocampal organization. We find novel evidence for a continuous gradient in the ERC, with greater autocorrelation in the posteromedial ERC and lower autocorrelation in the anterolateral ERC (Fig. 3). Lastly, the present study is the first to show that gradients of single voxel autocorrelation in the hippocampus are related to behavior during navigation. Specifically, autocorrelation in the anterior-medial hippocampus increased for difficult routes and was the greatest in the left hemisphere (Fig. 5), whereas autocorrelation in the posterior-lateral hippocampus was similar across routes. These findings support the functional organization gradient hypothesis that autocorrelation gradients are driven by intrinsic functional properties of the hippocampus and entorhinal cortex and suggest that these gradient patterns are not being driven by reciprocal connectivity or physiological noise (functional organization gradient; Fig. 1D).

Our data-driven approach, which allows voxels to cluster according to their single voxel autocorrelation, uncovered a multidimensional gradient in both the anterior–posterior and medial-lateral axes in both the hippocampus and ERC (Figs. 2 and 4). In the hippocampus, the anterior–posterior axis has been studied with respect to its role in representing graded information, for example coarse-grained to fine-grained information (Poppenk et al. 2013; Strange et al. 2014), large to small spatial distances (Evensmoen et al. 2013; Nielson et al. 2015; Peer et al. 2019), and long to short temporal distance (Nielson et al. 2015; Bellmund et al. 2019). Investigations of representational differences along the medial-lateral axis, however, have been limited because prior work has used predefined anatomical segmentations limited to the anterior and posterior portions of the long axis of the hippocampus. Our single voxel autocorrelation method is not restricted by predefined ROIs and proves to be a more precise measure that detects subtle differences in signal along the medial-lateral axis that have been previously overlooked and that are modulated by navigational difficulty. Moreover, our findings are consistent with recent evidence of an anterior-medial hippocampal cluster that has been identified in resting-state MRI studies (Dalton et al. 2021; Thorp et al. 2022) and functional fMRI studies, which find that the anterior-medial hippocampus plays a distinct role in a range of cognitive and episodic memory tasks (Addis et al. 2012; Lee et al. 2013; Zeidman et al. 2015; Zeidman and Maguire 2016; Dalton et al. 2018). In addition to the hippocampus, we found similar distinctions in the ERC. We observed a gradient of single voxel autocorrelation organization, such that greater single voxel autocorrelation was observed in the posterior-medial region and lower single voxel autocorrelation in the anterolateral region of the ERC (Fig. 3). This gradient is consistent with previous neuroimaging investigations of ERC which used high-resolution fMRI and functional connectivity to define distinct subregions within the human ERC (Maass et al. 2015; Navarro Schröder et al. 2015). Our analytic technique, however, goes beyond this prior work by demonstrating, for the first time, continuous gradients of autocorrelation in the ERC.

The present study demonstrates that the autocorrelation of the fMRI signal is not just global noise, but instead carries meaningful information about brain function that is directly related to behavior. Autocorrelation is frequently characterized as noise that masks meaningful signals and is unrelated to neuronal activity and cognition; therefore, we included steps in our analyses to control for noise and artifacts that might be driving the

autocorrelation signal (see Materials and Methods for details). A well-known source of autocorrelation of the fMRI signal comes from convolving the signal with the HRF (Friston et al. 1995). Recent research found that, while the autocorrelation signal mostly originates from the HRF, neural activity also contributes to the autocorrelation signal (Arbabshirani et al. 2019). Moreover, autocorrelation distinguished between global differences in cognitive state (task vs. rest) and mental state (healthy vs. schizophrenia) and these differences could not be accounted for solely by the HRF, physiological noise or motion (Arbabshirani et al. 2019). Moreover, the head motion control analysis of Dataset 2 demonstrated that differences in head motion across navigation conditions could not account for the differences in autocorrelation observed across navigation condition (see Supplementary Table S5). We therefore believe that the autocorrelation of the HRF or head motion alone cannot account for the findings presented here and that the autocorrelation is a measure of meaningful neural activity.

The interpretation of single voxel autocorrelation as a behaviorally relevant signal is corroborated by studies that use different measures of within-subject moment-to-moment signal and then relate these measures to cognitive performance. Specifically, research measuring changes in signal variability, as assessed by the standard deviation in BOLD signal over time, found that variability was related to task performance (see Garrett et al. 2013 for a review). For example, in younger adults, standard deviation of the BOLD signal was modulated by cognitive task demand, and as task difficulty increased, the variability decreased across the brain (Garrett et al. 2014). This finding is consistent with our findings from Dataset2, wherein increased autocorrelation (i.e. lower variability) was related to increases in navigational difficulty. Our technique goes beyond prior methods by measuring the stability of a single voxel's signal across multiple successive timepoints. This allows us to examine how the signal of individual voxels is maintained over an extended window of time and shows that this measure is directly related to behavior.

Recent research suggests that autocorrelation might be a global organizing principle and reflects intrinsic functional hierarchies in the brain (Irish and Vatansever 2020; Raut et al. 2020). For example, an analysis of resting state fMRI data calculated the autocorrelation decay in single voxels across a temporal window (0–8 s) and found a significant large-to-small timescale gradient along the anterior–posterior axis in the hippocampus (Raut et al. 2020), which is consistent with reports by Brunec, Bellana, et al. (2018). While current studies of autocorrelation cannot address the direct link between the autocorrelation gradients and behavior, our work suggests that autocorrelation can be used to discriminate between cognitive states that are uniform across the brain, leaving open the question of how autocorrelation gradients in specific brain regions might be related to differences in cognition during a behavioral task. Our analysis technique demonstrated novel gradients during resting state and can also be applied to task related activation to reveal their relation to on-going behavior and is the first to show that changes in single voxel autocorrelation gradients are directly related to changes in difficulty during a navigation task.

Anterior hippocampal voxels are more stable across time compared with the posterior hippocampus, which might enable the anterior hippocampus to maintain prior information across time during goal-directed navigation (Brunec, Bellana, et al. 2018). Our method proved to be a more sensitive measure than previous techniques (e.g. Brunec, Bellana, et al. 2018) because we were able to show differences in autocorrelation across navigation

conditions[2]. More specifically, we found that the autocorrelation in the anterior-medial hippocampus increased during navigation of difficult routes (Fig. 5). The autocorrelation signal may reflect the mechanism by which the hippocampus holds onto the past and carries it forward during navigation when we are in unfamiliar or unpredictable environments. For example, when navigating an unfamiliar route to a distant goal, the local details of the environment might not be helpful to orient oneself in relation to the goal; it may be more efficient, therefore, to keep in mind a coarser, overall map of the environment with information about steps already taken in order to reach the goal destination successfully. This large-scale representation may not be as useful to keep online during navigation of well-known or familiar routes where local details are sufficient for orienting and navigating to the goal, which could explain the decreased single voxel autocorrelation in the signal throughout the familiar routes (Fig. 5). This hypothesis is supported by previous research which has shown that the anterior hippocampus plays an important role in representing larger spatial and temporal distances (Evensmoen et al. 2013; Nielson et al. 2015) as well as representing coarser-grained, global representations (Collin et al. 2015).

We found that single voxel autocorrelation in the anterior-medial hippocampal cluster was higher in the left hemisphere compared with the right hemisphere (Fig. 5). It is still unclear whether this is representative of a stable difference in autocorrelation between the hemispheres or whether this reflects different types of information that are engaged across the two hemispheres during navigation. Future research is needed to determine the nature of this hemispheric difference.

Another nonmutually exclusive possibility is that the single voxel autocorrelation is representative of predictions that are cast into the future. The notion that increased temporal similarity is indicative of an extended spatiotemporal representation is supported by recent work investigating the predictive horizons along the hippocampal anteroposterior axis during navigation (Brunec and Momennejad 2022). Brunec and Momennejad (2022) found that as participants virtually navigated familiar, real-world routes (a subset of the familiar routes presented here), hippocampal activity was related to a hierarchical scale of horizon representations, in which the posterior hippocampus represented steps closer in the future trajectory (∼25 m), while the anterior hippocampus represented steps further in the future trajectory (∼175 m). It is possible, therefore, that the single voxel autocorrelation we observed helps represent an upcoming navigational trajectory, with immediate goals represented in posterior-lateral regions and more distal goals in the anterior-medial hippocampus. Our method and findings open the door for future studies using high-resolution neuroimaging in combination with a task

that parametrically modulates the amount of information that is carried over time in both predictable (familiar) and unpredictable (unfamiliar) environments to uncover content that is carried forward via the autocorrelation signal.

Although we were not able to relate the autocorrelation in ERC to behavior due to the resolution of the navigation data, if we apply the same logic we used for the hippocampus, our findings are consistent with the notion that alERC codes for local details and perceptual aspects of experience, whereas the pmERC codes for global contexts. Specifically, the (antero-)lateral ERC has been linked to fine-grained temporal processing (Tsao et al. 2018; Montchal et al. 2019) and to processing of object-context and within-object details (Yeung et al. 2017, 2019). The low autocorrelation we observed in the alERC might indicate faster updating of moment-to-moment changes and therefore support fine-grained representations. One caveat is that without analyses that directly relate the autocorrelation gradients in the entorhinal cortex to behavior, we cannot be sure whether the autocorrelation signal we observed in the entorhinal cortex supports low-to-high functional timescales. Future investigations using high-resolution scans can use our method to analyze continuous changes along both anterior–posterior and medial-lateral axes of the ERC without being restricted to anatomical subfield segmentations, perhaps revealing a more nuanced understanding of the organization of the ERC and relate it to behavior.

We observed three consistent ERC clusters in the right hemisphere and two consistent ERC clusters in the left hemisphere, suggesting that in this dataset, there was more variability in the left ERC intermediate cluster. We replicated this hemispheric asymmetry in both the left-to-right and right-to-left phase encoding direction datasets from Dataset1 (see Fig. 3B and Supplementary Fig. S3). These findings are interesting in light of the fact that there is some evidence that the human right ERC is larger than the left ERC (Insausti et al. 1998). Although the current work found hemispheric asymmetries in autocorrelation clustering with the resting state fMRI dataset (Dataset1, from the HCP), we did not find this same entorhinal asymmetry when we applied our single voxel autocorrelation method using a different dataset in which resting state scans were collected approximately 25 min after continuous θ-burst stimulation was applied to either the vertex (control site) or left angular gyrus (Coughlan et al. 2023). In this work, the autocorrelation clustering identified only two reliable clusters (one in anterolateral ERC and one in posteromedial ERC) in both the left and right ERC. One possible explanation for this discrepancy across these 2 papers is that the Dataset1 from the current work was collected at a higher resolution than the dataset from Coughlan et al. (2023). Using the higher resolution resting state scans might have enabled us to observe entorhinal hemispheric differences in autocorrelation clustering that did not show up in the lower resolution dataset. It is not clear yet whether the hemispheric asymmetry is a stable property of the left ERC. Future research is needed to determine whether signal dynamics in the left ERC are consistently different from those in the right ERC and whether there is a connection between the number of autocorrelation clusters generated and the volume of the left ERC.

It is currently unclear how the posterior-medial and anterior-lateral subregions of the ERC are functionally related to the anterior and posterior regions of the hippocampus. In the present study, we found that clusters in the anterior-medial hippocampus and posteromedial ERC had high single voxel autocorrelation, whereas clusters in the posterior-lateral hippocampus and anterolateral ERC had low single voxel autocorrelation.

---

[2] We directly compared our hippocampal autocorrelation clusters to the standard anatomical segmentations (head, body, tail) to determine whether our autocorrelation clusters explain more variance in the data than the standard anatomical ROIs. We found that whereas the head/body/tail anatomical segmentations capture some of the variance in autocorrelation along the anterior–posterior axis, the standard segmentations failed to capture critical relationships with behavior. Specifically, when using the anatomical ROIs, we do not observe the interaction between ROI and navigation condition, where autocorrelation in the anterior-medial hippocampus is greater for more difficult navigation conditions. The full analysis can be found in the Supplemental Materials (pp. 16–18). Moreover, we compared the effect size of the autocorrelation cluster labels to the effect size of the anatomical ROI labels and found a bigger effect size for the autocorrelation clusters compared with anatomical ROIs. Lastly, we directly compared two models of the single voxel autocorrelation throughout the hippocampus: one model included the autocorrelation clusters labels and the anatomical ROI labels as fixed effect predictors and the other model did not include autocorrelation cluster labels as a fixed effect predictor. We found that the model including autocorrelation cluster label explained the data better than the model with anatomical ROI alone (see Supplemental Materials pp. 16–18).

These distinctions along the anterior–posterior and medial-lateral axes of the ERC are consistent with previous functional connectivity findings (Navarro Schröder et al. 2015); however, functional connectivity and neuroanatomical studies in humans have been limited and do not find any clear differences between the anterior and posterior portions of the hippocampus with respect to their connectivity to different subregions in the ERC (Maass et al. 2015; Navarro Schröder et al. 2015; Syversen et al. 2021). Functional connections between these regions might be evident in the scale of information processing in the hippocampus and ERC. For example, it is possible that the pattern of low single voxel autocorrelation in anterolateral ERC and posterior-lateral hippocampus supports fine-grained processing—precise temporal processing in the anterolateral ERC (Bellmund et al. 2019; Montchal et al. 2019) and local spatial details in the posterior hippocampus (Doeller et al. 2008; Hirshhorn et al. 2012; Lee et al. 2012; Evensmoen et al. 2013).

There are currently no clear neuroanatomical links between the anterolateral ERC and posterior-lateral hippocampus or the anterior-medial hippocampus and posteromedial ERC. There are, however, probable connections between the anterior ERC and lateral hippocampus and posterior ERC with medial hippocampus (Strange et al. 2014; Witter et al. 2017; Nilssen et al. 2019; Witter and Amaral 2021). There is evidence that the temporal dynamics in the anterior-medial hippocampus and posteromedial ERC fluctuate together (Coughlan et al. 2023). Using the single voxel autocorrelation method described in this paper, Coughlan et al. (2023) demonstrated that when hippocampal-targeted transcranial magnetic stimulation is applied to the angular gyrus, the single voxel autocorrelation within the anterior-medial hippocampus and posteromedial ERC decreases. The decrease in single voxel autocorrelation within the anterior-medial hippocampus was also related to a decrease in functional connectivity to the angular gyrus (Coughlan et al. 2023). Our results, therefore, open the door for future investigations to characterize more fully the nature of anterior and posterior hippocampal signal dynamics in relation to the entorhinal subregions in humans and in relation to other structures, such as the angular gyrus (Coughlan et al. 2023), orbitofrontal cortex (Syversen et al. 2021), and prefrontal cortex (Barredo et al. 2015; Vaidya and Badre 2020).

The results presented here reveal 2 continuous gradients along the anterior–posterior and medial-lateral axes in the hippocampus and ERC. One outstanding question is whether there is new information that can be gained by investigating the two autocorrelation gradients separately, or whether the information they represent is redundant. Another outstanding question is whether our novel single voxel autocorrelation method can be applied with shorter timescales so that they can be used with event-related designs. Here, we use the entire timecourse of the voxel's activity to calculate the single voxel autocorrelation throughout the entire run, but it remains to be seen whether we can adapt our method to examine how autocorrelation changes over shorter time windows. This would allow us to ask new questions about what kind of information is being carried in the autocorrelation signal during discrete or shorter events and at event boundaries, which are known to trigger changes in hippocampal activity associated with integration of information across events (DuBrow and Davachi 2013; Ezzyat and Davachi 2014). Finally, this method can be used to investigate differences in autocorrelation within subfields of the hippocampus. For example, it has been proposed that CA1 is implicated in integrating information in memory, whereas DG/CA3, which mediates pattern separation, may be more implicated in making fine distinctions in memory

(Leutgeb et al. 2004; Yassa and Stark 2011; Kyle et al. 2015; Schapiro et al. 2017). Integration processes in CA1, therefore, might be supported by voxels with high single voxel autocorrelation, while separation processes in DG/CA3 might be better supported by low single voxel autocorrelation. Moreover, recent evidence also suggests that resting-state functional connectivity gradients in the hippocampus along the anterior–posterior and medial-lateral axes are closely associated with the microstructure of hippocampal subfields (Vos de Wael et al. 2018). Future research using our method and high-resolution fMRI is needed to test these differences within subfields.

Our studies were inspired initially by single-unit recording studies in rodents (Gothard et al. 1996; Maurer et al. 2005; Brun et al. 2008; Kjelstrup et al. 2008; Cavanagh et al. 2016). We believe our findings, however, have gone beyond replicating the rodent findings in humans, a worthy task in its own right, but extended the findings to the point that they can now be used to inform future studies in rodents and humans. We provide some examples in which this is the case. For example, our method enabled us to find differences in autocorrelation along the anterior–posterior and medial-lateral axes in the entorhinal cortex, which have only been examined in a restricted region in rodents (Brun et al. 2008). Our findings are consistent with neuroanatomical and neuro-physiological divisions in that structure (human: Maass et al. 2015; monkey: Witter and Amaral 2021; rat: Witter et al. 2017). Furthermore, our findings are consistent with recent evidence from resting-state fMRI of 2 functional connectivity gradients in the hippocampus: a primary gradient along the anterior–posterior axis and a secondary gradient along the medial-lateral axis (Vos de Wael et al. 2018). Although activity of a single voxel that is comprised of thousands of neurons may be considered to be a coarser unit of analysis than recordings from single units, it may be the case that it is the operation of a population of these neurons that is most closely linked to organizational temporal dynamics. It is the gradients revealed by autocorrelation at the single voxel level that enabled us to link hippocampal dynamics to behavior. In addition, we were able to segment the populations into clusters, suggesting subdivisions that would not be evident at the single-unit level. It would be worthwhile to determine whether similar clusters are found in rodents and examine their functional significance. Similar analyses at the population-level in rodents may yield information about the relation of neural dynamics to higher level memory representations and goals, an enterprise that is just beginning (Morrissey et al. 2017; Jacob and Josselyn 2020).

Limitations

We observed considerable spatial variability in Cluster 2 (as indicated by the small Jaccard coefficients), which was evident both across individuals as well as across runs within individuals. One interesting hypothesis is that this variability reflects fundamental flexibility in the representational properties of this "intermediate" hippocampal region (Fanselow and Dong 2010). That is, Cluster 2 voxels may adjust their temporal dynamics to be more like Cluster 1 or Cluster 3 depending on the nature of the task. While there may be underlying functional or biological properties of Cluster 2 that make it distinct from Cluster 1 and 3, the low reliability of Cluster 2 voxels within individuals makes this hypothesis challenging to assess in the current study. To properly test whether Cluster 2 voxels flexibly adjust their temporal dynamics based on task demands, a future study could design two different tasks: one that would preferentially engage the posterior hippocampus and one that would preferentially engage the anterior hippocampus. We could then measure the change in spatial distribution of

Cluster 1 and 3 across both tasks. Evidence in support of a representationally flexible intermediate hippocampal region would be finding that voxels in the intermediate hippocampus change to look Cluster 3 during a task that preferentially engages the posterior hippocampus (Cluster 3) and that these same voxels then shift to look more such as Cluster 1 during a task that preferentially engages the anterior hippocampus (Cluster 1). Additionally, research investigating the cytoarchitectonic structure of the primate neocortex suggests that transitions between different brain areas are continuous and there are not discrete boarders between areas (Rockel et al. 1980). In the present work, we assign each voxel a single label; however, one voxel can contain information from different brain areas. This spatial limitation of fMRI makes it difficult to know whether the discrete transitions we observed between clusters actually reflect the underlying cytoarchitectonic gradient that is inherent to the hippocampal and entorhinal structures or whether it is the result of forcing each voxel to be assigned to a single cluster. Future research is needed to further characterize the intermediate regions of the hippocampus and entorhinal cortex.

Another limitation of the present study is that it remains unclear whether these gradients of autocorrelation are found throughout the brain or if they are unique to the hippocampus and entorhinal cortex. In order to develop this new technique, we focused our analyses on the hippocampus and entorhinal cortex because we had strong predictions about the gradients we might observe in the these regions based on the underlying neural signals evident from single unit recordings in rodents and previous fMRI studies in humans (Jung et al. 1994; Hasselmo 2008; Kjelstrup et al. 2008; Komorowski et al. 2013; Evensmoen et al. 2015; Maass et al. 2015; Navarro Schröder et al. 2015; Syversen et al. 2021). Moreover, a recent study has examined the autocorrelation of individual voxels across the whole brain (Raut et al. 2020). They found cortical and subcortical hierarchical gradient across the brain that were related to the organization of functional networks. Networks associated with faster processing timescales (e.g. motor, visual, cingulo-percular) had lower autocorrelation, while networks associated with slower processing timescales (dorsal attention, frontoparietal control, default mode). They also examined the hippocampus and found a gradient of autocorrelation similar to the results presented in this paper—an increase of low-to-high autocorrelation extending from the posterior to anterior hippocampus. Future research using our method can examine single voxel autocorrelation gradients throughout the brain and test whether they are modulated by behavior. This work can help our understanding of how single voxel autocorrelation is related to the underlying biological neural signals and the functional processes related to other brain regions and networks.

Conclusion

Our results provide compelling evidence for a gradation of single voxel autocorrelation in the hippocampus and ERC. Our single voxel method proved to be a fine-grained measure that revealed subtleties in the spatial organization of autocorrelation, going beyond prior methods, and allowed us to observe graded signals along anterior–posterior and medial-lateral axes in both regions. Furthermore, we show for the first time that differences in single voxel autocorrelation gradients in the hippocampus can be directly related to differences in difficulty during a virtual navigation task, thus opening the door for future research to ask new questions of the autocorrelation signal and uncover how it is related to behavior.

Acknowledgments

Supplementary material

Supplementary material is available at *Cerebral Cortex* online.

Funding

References

Addis DR, Knapp K, Roberts RP, Schacter DL. Routes to the past: neural substrates of direct and generative autobiographical memory retrieval. *NeuroImage*. 2012:59(3):2908–2922. https://doi.org/10.1016/j.neuroimage.2011.09.066.

Arbabshirani MR, Damaraju E, Phlypo R, Plis S, Allen E, Ma S, Mathalon D, Calhoun VD. Impact of autocorrelation on functional connectivity. *NeuroImage*. 2014:102(part 2):294–308. https://doi.org/10.1016/j.neuroimage.2014.07.045.

Arbabshirani MR, Preda A, Vaidya JG, Potkin SG, Pearlson G, Voyvodic J, Mathalon D, van Erp T, Michael A, Kiehl KA, et al. Autoconnectivity: a new perspective on human brain function. *J Neurosci Methods*. 2019:323(15):68–76. https://doi.org/10.1016/j.jneumeth.2019.03.015.

Barr DJ, Levy R, Scheepers C, Tily HJ. Random effects structure for confirmatory hypothesis testing: keep it maximal. *J Mem Lang*. 2013:68(3):255–278.

Barredo J, Öztekin I, Badre D. Ventral fronto-temporal pathway supporting cognitive control of episodic memory retrieval. *Cereb Cortex*. 2015:25(4):1004–1019.

Bellmund JL, Deuker L, Schröder TN, Doeller CF. *Grid-cell representations in mental simulation*, Elife. 2016:5:e17089. https://doi.org/10.7554/eLife.17089.

Bellmund JL, Deuker L, Doeller CF. Mapping sequence structure in the human lateral entorhinal cortex. *Elife*. 2019:8:e45333. https://doi.org/10.7554/eLife.45333.

Berron D, Neumann K, Maass A, Schütze H, Fliessbach K, Kiven V, Jessen F, Sauvage M, Kumaran D, Düzel E. Age-related functional changes in domain-specific medial temporal lobe pathways. *Neurobiol Aging*. 2018:65:86–97. https://doi.org/10.1016/j.neurobiolaging.2017.12.030.

Blondel VD, Guillaume J-L, Lambiotte R, Lefebvre E. Fast unfolding of communities in large networks. *J Stat Mech Theory Exp*. 2008:2008:P10008. https://doi.org/10.1088/1742-5468/2008/10/p10008.

Bollmann S, Puckett AM, Cunnington R, Barth M. Serial correlations in single-subject fMRI with sub-second TR. *NeuroImage*. 2018:166(1):152–166. https://doi.org/10.1016/j.neuroimage.2017.10.043.

Brun VH, Solstad T, Kjelstrup KB, Fyhn M, Witter MP, Moser EI, Moser MB. Progressive increase in grid scale from dorsal to ventral medial entorhinal cortex. *Hippocampus*. 2008:18(12):1200–1212.

Brunec IK, Momennejad I. Predictive representations in hippocampal and prefrontal hierarchies. *J Neurosci*. 2022:42(2):299–312. https://doi.org/10.1523/JNEUROSCI.1327-21.2021.

Brunec IK, Bellana B, Ozubko JD, Man V, Robin J, Liu ZX, Grady C, Rosenbaum RS, Winocur G, Barense MD, et al. Multiple scales of representation along the hippocampal anteroposterior axis in humans. *Curr Biol*. 2018:28(13):2129–2135.e6. https://doi.org/10.1016/j.cub.2018.05.016.

Bullmore E, Long C, Suckling J, Fadili J, Calvert G, Zelaya F, Brammer M. Colored noise and computational inference in neurophysiological (fMRI) time series analysis: resampling methods in time and wavelet domains. *Hum Brain Mapp*. 2001:12(2):61–78.

Campbell K, Grigg O, Saverino C, Churchill N, Grady C. Age differences in the intrinsic functional connectivity of default network subsystems. *Front Aging Neurosci*. 2013:5:73. https://doi.org/10.3389/fnagi.2013.00073.

Cavanagh SE, Wallis JD, Kennerley SW, Hunt LT. Autocorrelation structure at rest predicts value correlates of single neurons during reward-guided choice. *Elife*. 2016:5:e18937. https://doi.org/10.7554/eLife.18937.

Collin SH, Milivojevic B, Doeller CF. Memory hierarchies map onto the hippocampal long axis in humans. *Nat Neurosci*. 2015:18(11):1562–1564. https://doi.org/10.1038/nn.4138.

Coughlan G, Bouffard NR, Golestani A, Thakral PP, Schacter DL, Grady C, Moscovitch M. Transcranial magnetic stimulation to the angular gyrus modulates the temporal dynamics of the hippocampus and entorhinal cortex. *Cereb Cortex*. 2023:36(6):3255–3264. https://doi.org/10.1093/cercor/bhac273.

Cox RW. AFNI: software for analysis and visualization of functional magnetic resonance neuroimages. *Comput Biomed Res*. 1996:29(3):162–173.

Dalmaijer ES, Nord CL, Astle DE. Statistical power for cluster analysis. *BMC Bioinform*. 2022:23(1):1–28.

Dalton MA, Zeidman P, McCormick C, Maguire EA. Differentiable processing of objects, associations, and scenes within the hippocampus. *J Neurosci*. 2018:38(38):8146–8159. https://doi.org/10.1523/JNEUROSCI.0263-18.2018.

Dalton MA, McCormick C, Maguire EA. Differences in functional connectivity along the anterior-posterior axis of human hippocampal subfields. *NeuroImage*. 2019:192:38–51. https://doi.org/10.1016/j.neuroimage.2019.02.066.

Dalton MA, D'Souza A, Lv J, Calamante F. New insights into anatomical connectivity along the anterior–posterior axis of the human hippocampus using in vivo quantitative fibre tracking. *Elife*. 2022:11:e76143. https://doi.org/10.7554/eLife.76143.

Doeller CF, King JA, Burgess N. Parallel striatal and hippocampal systems for landmarks and boundaries in spatial memory.

Proc Natl Acad Sci. 2008:105(15):5915–5920. https://doi.org/10.1073/pnas.0801489105.

DuBrow S, Davachi L. The influence of context boundaries on memory for the sequential order of events. *J Exp Psychol Gen*. 2013:142(4):1277–1286. https://doi.org/10.1037/a0034024.

Evensmoen HR, Lehn H, Xu J, Witter MP, Nadel L, Håberg AK. The anterior hippocampus supports a coarse, global environmental representation and the posterior hippocampus supports fine-grained, local environmental representations. *J Cogn Neurosci*. 2013:25(11):1908–1925. https://doi.org/10.1162/jocn_a_00436.

Evensmoen HR, Ladstein J, Hansen TI, Møller JA, Witter MP, Nadel L, Håberg AK. From details to large scale: the representation of environmental positions follows a granularity gradient along the human hippocampal and entorhinal anterior–posterior axis. *Hippocampus*. 2015:25(1):119–135.

Ezzyat Y, Davachi L. Similarity breeds proximity: pattern similarity within and across contexts is related to later mnemonic judgments of temporal proximity. *Neuron*. 2014:81(5):1179–1189. https://doi.org/10.1016/j.neuron.2014.01.042.

Fanselow MS, Dong HW. Are the dorsal and ventral hippocampus functionally distinct structures? *Neuron*. 2010:65(1):7–19.

Friston KJ, Holmes AP, Poline JB, Grasby PJ, Williams SCR, Frackowiak RS, Turner R. Analysis of fMRI time-series revisited. *NeuroImage*. 1995:2(1):45–53. https://doi.org/10.1006/nimg.1995.1007.

Garrett DD, Samanez-Larkin GR, MacDonald SW, Lindenberger U, McIntosh AR, Grady CL. Moment-to-moment brain signal variability: a next frontier in human brain mapping? *Neurosci Biobehav Rev*. 2013:37(4):610–624. https://doi.org/10.1016/j.neubiorev.2013.02.015.

Garrett DD, McIntosh AR, Grady CL. Brain signal variability is parametrically modifiable. *Cereb Cortex*. 2014:24(11):2931–2940. https://doi.org/10.1093/cercor/bht150.

Genon S, Bernhardt BC, La Joie R, Amunts K, Eickhoff SB. The many dimensions of human hippocampal organization and (dys) function. *Trends Neurosci*. 2021:44(12):977–989. https://doi.org/10.1016/j.tins.2021.10.003.

Glasser MF, Sotiropoulos SN, Wilson JA, Coalson TS, Fischl B, Andersson JL, Xu J, Jbabdi S, Webster M, et al. The minimal preprocessing pipelines for the Human Connectome Project. *NeuroImage*. 2013:80:105–124. https://doi.org/10.1016/j.neuroimage.2013.04.127.

Glasser MF, Smith SM, Marcus DS, Andersson JL, Auerbach EJ, Behrens TE, Coalson TS, Harms MP, Jenkinson M, Moeller S, et al. The human connectome project's neuroimaging approach. *Nat Neurosci*. 2016:19(9):1175–1187. https://doi.org/10.1038/nn.4361.

Gothard KM, Skaggs WE, McNaughton BL. Dynamics of mismatch correction in the hippocampal ensemble code for space: interaction between path integration and environmental cues. *J Neurosci*. 1996:16(24):8027–8040. https://doi.org/10.1523/JNEUROSCI.16-24-08027.1996.

Grady CL. Meta-analytic and functional connectivity evidence from functional magnetic resonance imaging for an anterior to posterior gradient of function along the hippocampal axis. *Hippocampus*. 2020:30(5):456–471. https://doi.org/10.1002/hipo.23164.

Griffanti L, Salimi-Khorshidi G, Beckmann CF, Auerbach EJ, Douaud G, Sexton CE, Zsoldos E, Ebmeier KP, Filippini N, Mackay CE, et al. ICA-based artefact removal and accelerated fMRI acquisition for improved resting state network imaging. *NeuroImage*. 2014:95:232–247. https://doi.org/10.1016/j.neuroimage.2014.03.034.

Hafting T, Fyhn M, Molden S, Moser MB, Moser EI. Microstructure of a spatial map in the entorhinal cortex. *Nature*. 2005:436(7052): 801–806. https://doi.org/10.1038/nature03721.

Hasselmo ME. Grid cell mechanisms and function: contributions of entorhinal persistent spiking and phase resetting. *Hippocampus*. 2008:18(12):1213–1229. https://doi.org/10.1002/hipo.20512.

He BJ. Scale-free brain activity: past, present, and future. *Trends Cogn Sci*. 2014:18(9):480–487. https://doi.org/10.1016/j.tics.2014.04.003.

Hirshhorn M, Grady C, Rosenbaum RS, Winocur G, Moscovitch M. Brain regions involved in the retrieval of spatial and episodic details associated with a familiar environment: an fMRI study. *Neuropsychologia*. 2012:50(13):3094–3106. https://doi.org/10.1016/j.neuropsychologia.2012.08.008.

Hrybouski S, MacGillivray M, Huang Y, Madan CR, Carter R, Seres P, Malykhin NV. Involvement of hippocampal subfields and anterior-posterior subregions in encoding and retrieval of item, spatial, and associative memories: longitudinal versus transverse axis. *NeuroImage*. 2019:191(1):568–586. https://doi.org/10.1016/j.neuroimage.2019.01.061.

Hutton C, Josephs O, Stadler J, Featherstone E, Reid A, Speck O, Bernarding J, Weiskopf N. The impact of physiological noise correction on fMRI at 7T. *NeuroImage*. 2011:57(1):101–112. https://doi.org/10.1016/j.neuroimage.2011.04.018.

Igarashi KM, Ito HT, Moser EI, Moser MB. Functional diversity along the transverse axis of hippocampal area CA1. *FEBS Lett*. 2014:588(15):2470–2476. https://doi.org/10.1016/j.febslet.2014.06.004.

Insausti R, Juottonen K, Soininen H, Insausti AM, Partanen K, Vainio P, Laakso MP, Pitkänen A. MR volumetric analysis of the human entorhinal, perirhinal, and temporopolar cortices. *Am J Neuroradiol*. 1998:19(4):659–671.

Irish M, Vatansever D. Rethinking the episodic-semantic distinction from a gradient perspective. *Curr Opin Behav Sci*. 2020:32:43–49. https://doi.org/10.1016/j.cobeha.2020.01.016.

Jacob AD, Josselyn SA. Why have two when one will do? Comparing task representations across amygdala and prefrontal cortex in single neurons and neuronal populations. *Neuron*. 2020:107(4):597–599. https://doi.org/10.1016/j.neuron.2020.07.038.

James O, Park H, Kim SG. Impact of sampling rate on statistical significance for single subject fMRI connectivity analysis. *Hum Brain Mapp*. 2019:40(11):3321–3337. https://doi.org/10.1002/hbm.24600.

Jung MW, Wiener SI, McNaughton BL. Comparison of spatial firing characteristics of units in dorsal and ventral hippocampus of the rat. *J Neurosci*. 1994:14(12):7347–7356.

Kjelstrup KB, Solstad T, Brun VH, Hafting T, Leutgeb S, Witter MP, Moser MB. Finite scale of spatial representation in the hippocampus. *Science*. 2008:321(5885):140–143. https://doi.org/10.1126/science.1157086.

Komorowski RW, Garcia CG, Wilson A, Hattori S, Howard MW, Eichenbaum H. Ventral hippocampal neurons are shaped by experience to represent behaviorally relevant contexts. *J Neurosci*. 2013:33(18):8079–8087. https://doi.org/10.1523/JNEUROSCI.5458-12.2013.

Kyle CT, Stokes JD, Lieberman JS, Hassan AS, Ekstrom AD. Successful retrieval of competing spatial environments in humans involves hippocampal pattern separation mechanisms. *elife*. 2015:4:e10499. https://doi.org/10.7554/eLife.10499.

Laurens R. K. (2021). *Permutation test*. GitHub. Retrieved 2021 February 16 https://github.com/lrkrol/permutationTest.

Lee AC, Yeung LK, Barense MD. The hippocampus and visual perception. *Front Hum Neurosci*. 2012:6:91. https://doi.org/10.3389/fnhum.2012.00091.

Lee AC, Brodersen KH, Rudebeck SR. Disentangling spatial perception and spatial memory in the hippocampus: a univariate and multivariate pattern analysis fMRI study. *J Cogn Neurosci*. 2013:25(4): 534–546. https://doi.org/10.1162/jocn_a_00301.

Lenoski B, Baxter LC, Karam LJ, Maisog J, Debbins J. On the performance of autocorrelation estimation algorithms for fMRI analysis. *IEEE J Sel Top Signal Process*. 2008:2(6):828–838. https://doi.org/10.1109/jstsp.2008.2007819.

Leutgeb S, Leutgeb JK, Treves A, Moser MB, Moser EI. Distinct ensemble codes in hippocampal areas CA3 and CA1. *Science*. 2004:305(5688):1295–1298. https://doi.org/10.1126/science.1100265.

López-Madrona VJ, Matias FS, Mirasso CR, Canals S, Pereda E. Inferring correlations associated to causal interactions in brain signals using autoregressive models. *Sci Rep*. 2019:9(1):17041. https://doi.org/10.1038/s41598-019-53453-2.

Lund TE, Madsen KH, Sidaros K, Luo WL, Nichols TE. Non-white noise in fMRI: does modelling have an impact? *NeuroImage*. 2006:29(1): 54–66. https://doi.org/10.1016/j.neuroimage.2005.07.005.

Maass A, Berron D, Libby LA, Ranganath C, Düzel E. Functional subregions of the human entorhinal cortex. *Elife*. 2015:4:e06426. https://doi.org/10.7554/eLife.06426.

Maurer AP, VanRhoads SR, Sutherland GR, Lipa P, McNaughton BL. Self-motion and the origin of differential spatial scaling along the septo-temporal axis of the hippocampus. *Hippocampus*. 2005:15(7):841–852. https://doi.org/10.1002/hipo.20114.

Montchal ME, Reagh ZM, Yassa MA. Precise temporal memories are supported by the lateral entorhinal cortex in humans. *Nat Neurosci*. 2019:22(2):284–288. https://doi.org/10.1038/s41593-018-0303-1.

Morrissey MD, Insel N, Takehara-Nishiuchi K. Generalizable knowledge outweighs incidental details in prefrontal ensemble code over time. *elife*. 2017:6:e22177. https://doi.org/10.7554/eLife.22177.

Nadel L, Hoscheidt S, Ryan LR. Spatial cognition and the hippocampus: the anterior–posterior axis. *J Cogn Neurosci*. 2013:25(1):22–28. https://doi.org/10.1162/jocn_a_00313.

Navarro Schröder T, Haak KV, Jimenez NIZ, Beckmann CF, Doeller CF. Functional topography of the human entorhinal cortex. *Elife*. 2015:4:e06738. https://doi.org/10.7554/eLife.06738.

Nielson DM, Smith TA, Sreekumar V, Dennis S, Sederberg PB. Human hippocampus represents space and time during retrieval of real-world memories. *Proc Natl Acad Sci*. 2015:112(35):11078–11083. https://doi.org/10.1073/pnas.1507104112.

Nilssen ES, Doan TP, Nigro MJ, Ohara S, Witter MP. Neurons and networks in the entorhinal cortex: a reappraisal of the lateral and medial entorhinal subdivisions mediating parallel cortical pathways. *Hippocampus*. 2019:29(12):1238–1254. https://doi.org/10.1002/hipo.23145.

Olsen RK, Yeung LK, Noly-Gandon A, D'Angelo MC, Kacollja A, Smith VM, Barense MD. Human anterolateral entorhinal cortex volumes are associated with cognitive decline in aging prior to clinical diagnosis. *Neurobiol Aging*. 2017:57:195–205. https://doi.org/10.1016/j.neurobiolaging.2017.04.025.

Peer M, Ron Y, Monsa R, Arzy S. Processing of different spatial scales in the human brain. *Elife*. 2019:8:e47492. https://doi.org/10.7554/eLife.47492.

Poppenk J, Evensmoen HR, Moscovitch M, Nadel L. Long-axis specialization of the human hippocampus. *Trends Cogn Sci*. 2013:17(5): 230–240. https://doi.org/10.1016/j.tics.2013.03.005.

Power JD, Barnes KA, Snyder AZ, Schlaggar BL, Petersen SE. Spurious but systematic correlations in functional connectivity MRI networks arise from subject motion. *NeuroImage*. 2012:59(3):2142–2154. https://doi.org/10.1016/j.neuroimage.2011.10.018.

Purdon PL, Weisskoff RM. Effect of temporal autocorrelation due to physiological noise and stimulus paradigm on voxel-level false-positive rates in fMRI. *Hum Brain Mapp*. 1998:6(4):239–249. https://doi.org/10.1002/(SICI)1097-0193(1998)6:4<239::AID-HBM4>3.0.CO;2-4.

R Core Team. *R: a language and environment for statistical computing*. Vienna, Austria: R Foundation for Statistical Computing; 2019. https://www.R-project.org/

Rajapakse JC, Kruggel F, Maisog JM, Yves von Cramon D. Modeling hemodynamic response for analysis of functional MRI time-series. *Hum Brain Mapp*. 1998:6(4):283–300.

Raut RV, Snyder AZ, Raichle ME. Hierarchical dynamics as a macroscopic organizing principle of the human brain. *Proc Natl Acad Sci*. 2020:117(34):20890–20897. https://doi.org/10.1073/pnas.2003383117.

Ritchey M, Montchal ME, Yonelinas AP, Ranganath C. Delay-dependent contributions of medial temporal lobe regions to episodic memory retrieval. *Elife*. 2015:4:e05025. https://doi.org/10.7554/eLife.05025.

Robin J, Moscovitch M. Details, gist and schema: hippocampal–neocortical interactions underlying recent and remote episodic and spatial memory. *Curr Opin Behav Sci*. 2017:17:114–123. https://doi.org/10.1016/j.cobeha.2017.07.016.

Rockel AJ, Hiorns RW, Powell TP. The basic uniformity in structure of the neocortex. *Brain J Neurol*. 1980:103(2):221–244.

Salimi-Khorshidi G, Douaud G, Beckmann CF, Glasser MF, Griffanti L, Smith SM. Automatic denoising of functional MRI data: combining independent component analysis and hierarchical fusion of classifiers. *NeuroImage*. 2014:90:449–468. https://doi.org/10.1016/j.neuroimage.2013.11.046.

Sasaki T, Leutgeb S, Leutgeb JK. Spatial and memory circuits in the medial entorhinal cortex. *Curr Opin Neurobiol*. 2015:32:16–23. https://doi.org/10.1016/j.conb.2014.10.008.

Schapiro AC, Turk-Browne NB, Botvinick MM, Norman KA. Complementary learning systems within the hippocampus: a neural network modelling approach to reconciling episodic memory with statistical learning. *Philos Trans R Soc B Biol Sci*. 2017:372(1711):20160049.

Singmann H, Kellen D. An introduction to mixed models for experimental psychology. In: Spieler DH, Schumacher E, editors. *New methods in cognitive psychology*. Routledge: Psychology Press; 2019. pp. 4–31.

Singmann, H., Bolker, B., Westfall, J., Aust, F., & Ben-Shachar, M. S. (2020). *afex: analysis of factorial experiments*. R package version 0.28-0. https://CRAN.R-project.org/package=afex

Small SA, Schobel SA, Buxton RB, Witter MP, Barnes CA. A pathophysiological framework of hippocampal dysfunction in ageing and disease. *Nat Rev Neurosci*. 2011:12(10):585–601. https://doi.org/10.1038/nrn3085.

[dataset] Smith SM, Beckmann CF, Andersson J, Auerbach EJ, Bijsterbosch J, Douaud G, Duff E, Feinberg DA, Griffanti L, et al. Resting-state fMRI in the human connectome project. *NeuroImage*. 2013:80:144–168. https://doi.org/10.1016/j.neuroimage.2013.05.039.

Strange BA, Witter MP, Lein ES, Moser EI. Functional organization of the hippocampal longitudinal axis. *Nat Rev Neurosci*. 2014:15(10):655–669. https://doi.org/10.1038/nrn3785.

Syversen IF, Witter MP, Kobro-Flatmoen A, Goa PE, Schröder TN, Doeller CF. Structural connectivity-based segmentation of the human entorhinal cortex. *NeuroImage*. 2021:245:118723.

Thorp JN, Gasser C, Blessing EM, Davachi L. Data-Driven Clustering of Functional Signals Reveals Gradients in Processing Both within the Anterior Hippocampus and across Its Long Axis. *J Neurosci*. 2022:42(39):7431–7441. https://doi.org/10.1523/JNEUROSCI.0269-22.2022.

Tsao A, Sugar J, Lu L, Wang C, Knierim JJ, Moser MB, Moser EI. Integrating time from experience in the lateral entorhinal cortex. *Nature*. 2018:561(7721):57–62. https://doi.org/10.1038/s41586-018-0459-6.

Vaidya AR, Badre D. Neural systems for memory-based value judgment and decision-making. *J Cogn Neurosci*. 2020:32(10):1896–1923. https://doi.org/10.1162/jocn_a_01595.

Van Essen DC, Smith SM, Barch DM, Behrens TE, Yacoub E, Ugurbil K, Wu-Minn HCP Consortium. The WU-Minn human connectome project: an overview. *NeuroImage*. 2013:80:62–79. https://doi.org/10.1016/j.neuroimage.2013.05.041.

Vos de Wael R, Larivière S, Caldairou B, Hong SJ, Margulies DS, Jefferies E, Bernasconi A, Smallwood J, Bernasconi N, Bernhardt BC. Anatomical and microstructural determinants of hippocampal subfield functional connectome embedding. *Proc Natl Acad Sci*. 2018:115(40):10154–10159. https://doi.org/10.1073/pnas.1803667115.

Wickham, H. (2017). *tidyverse: easily install and load the 'Tidyverse'*. R package version 1.2.1. https://CRAN.R-project.org/package=tidyverse

Wickramaarachchi, C., Frincu, M., Small, P., & Prasanna, V. K. (2014) Fast parallel algorithm for unfolding of communities in large graphs. In: *2014 IEEE High Performance Extreme Computing Conference (HPEC)* (pp. 1–6). IEEE. https://doi.org/10.1109/hpec.2014.7040973.

Witter MP, Amaral DG. The entorhinal cortex of the monkey: VI. Organization of projections from the hippocampus, subiculum, presubiculum, and parasubiculum. *J Comp Neurol*. 2021:529(4):828–852. https://doi.org/10.1002/cne.24983.

Witter MP, Doan TP, Jacobsen B, Nilssen ES, Ohara S. Architecture of the entorhinal cortex a review of entorhinal anatomy in rodents with some comparative notes. *Front Syst Neurosci*. 2017:11:46. https://doi.org/10.3389/fnsys.2017.00046.

Yassa MA, Stark CE. Pattern separation in the hippocampus. *Trends Neurosci*. 2011:34(10):515–525. https://doi.org/10.1016/j.tins.2011.06.006.

Yeung LK, Olsen RK, Bild-Enkin HE, D'Angelo MC, Kacollja A, McQuiggan DA, Keshabyan A, Ryan JD, Barense MD. Anterolateral entorhinal cortex volume predicted by altered intra-item configural processing. *J Neurosci*. 2017:37(22):5527–5538. https://doi.org/10.1523/JNEUROSCI.3664-16.2017.

Yeung LK, Olsen RK, Hong B, Mihajlovic V, D'Angelo MC, Kacollja A, Ryan JD, Barense MD. Object-in-place memory predicted by anterolateral entorhinal cortex and parahippocampal cortex volume in older adults. *J Cogn Neurosci*. 2019:31(5):711–729. https://doi.org/10.1162/jocn_a_01385.

Zeidman P, Maguire EA. Anterior hippocampus: the anatomy of perception, imagination and episodic memory. *Nat Rev Neurosci*. 2016:17(3):173–182. https://doi.org/10.1038/nrn.2015.24.

Zeidman P, Mullally SL, Maguire EA. Constructing, perceiving, and maintaining scenes: hippocampal activity and connectivity. *Cereb Cortex*. 2015:25(10):3836–3855. https://doi.org/10.1093/cercor/bhu266.